JOURNAL OF SPACECRAFT AND ROCKETS
Vol. 45, No. 4, July–August 2008

Simulation of a Flush Air-Data System for Transatmospheric Vehicles

Joel C. Ellsworth* and Stephen A. Whitmore†
Utah State University, Logan, Utah 84322-4130

DOI: 10.2514/1.33541

Design of flush air-data sensing system based on the X-34 outer mold line is presented. The X-34 is chosen for this study because it incorporates many of the features needed by a commercial suborbital-tourist spaceflight operation and the aerodynamic database is available in the public domain. The X-34 flush air-data sensing system uses a cluster of nose-mounted pressure orifices to estimate air-data parameters. For this study, a typical X-34 trajectory is used to generate simulated nosecap surface-pressure values based on wind-tunnel-derived calibration models. Pressures are corrupted with various noise models and processed by a solver algorithm for the flush air-data sensing system to obtain air-data estimates. Residuals are used to analyze system performance. For reentry conditions at high altitudes and Mach numbers, for which the flush air-data sensing system has its greatest operational benefit, very low ambient pressure levels result in an unacceptable signal-to-noise ratio. The operational range of the system is extended to very high altitudes by using a complementary filter to blend inertially derived air data with the sensed pressure data of the flush air-data sensing system. Details and sample results from the complementary algorithm are presented. The coupled flush air-data sensing system and inertial algorithm results in a clean unbiased output throughout the entire endoatmospheric flight path, including launch, reentry, approach, and landing.

Nomenclature

A	=	quadratic-equation parameter, logistical population parameter
A_c	=	tube cross-sectional area, cm^2
A_{mpl}	=	logistical growth parameter amplitude
A_{wght}	=	complementary filter FADS system health weighting parameter
B	=	quadratic-equation parameter
C	=	quadratic-equation parameter, logistical offset parameter
C_p	=	specific heat at constant pressure, $\text{kJ/kg} - \text{K}$
C_p	=	pressure ratio
c_1	=	logistical gain-schedule time-axis parameter
D	=	tube diameter, cm
F	=	pressure model function, kPa
FADS	=	parameters derived from the flush air-data sensing system
h_p	=	pressure altitude, km
i	=	port index
inertial	=	inertially derived parameter
j	=	port index
k	=	port index, time index
L	=	pneumatic tubing length, m
M_∞	=	freestream Mach number
n	=	number of pressure ports
P_L	=	sensed pressure at transducer, kPa
P_0	=	input pressure to pneumatic tubing, kPa
p	=	flush air-data sensing system surface pressure, kPa
p_{02}	=	total pressure behind the bow shock wave, kPa
p_∞	=	freestream static pressure, kPa
Q	=	weighting matrix
q	=	weighting matrix element
qc_2	=	dynamic pressure behind the bow shock wave, kPa
R	=	logistical growth rate
s	=	sample variance
s	=	Laplace variable, 1/s
T_{ref}	=	reference temperature calculated from Eckert's formula, K
Ta_{wall}	=	adiabatic wall temperature, K
$T0_2$	=	stagnation temperature behind the bow shock, K
T_2	=	static gas temperature behind the bow shock, K
T_∞	=	freestream temperature, K
U	=	axial velocity component, m/s
u	=	nondimensional axial velocity component
V	=	entrapped volume in pressure transducer, cm^3
V	=	lateral velocity component, m/s
v	=	nondimensional lateral velocity component
W	=	normal velocity component, m/s
w	=	nondimensional normal velocity component
X	=	axial port coordinate, sample value, m
X_{FADS}	=	air-data state vector
x	=	nondimensional axial port coordinate, sample value
Y	=	lateral port coordinate, m
y	=	nondimensional lateral port coordinate
Z	=	normal port coordinate, m
z	=	nondimensional normal port coordinate
z	=	discrete-time Laplace variable, 1/s
α	=	indicated angle of attack, deg
β	=	indicated angle of sideslip, deg
Γ	=	pressure parameter, kPa
Γ	=	gamma function,
γ	=	ratio of specific heats
Δt	=	sample interval, s
δ	=	shock wave standoff distance, cm
δp	=	flush air-data sensing system pressure residual
$\delta\alpha$	=	angle-of-attack calibration value, deg
$\delta\beta$	=	angle-of-sideslip calibration value, deg
ε	=	compressibility correction
ζ	=	damping ratio of the port response function
Θ	=	incidence angle parameter
θ	=	local surface incidence angle, deg
κ	=	thermal conductivity, $\text{W/m} - \text{K}$
κ	=	degrees of freedom

Presented as Paper 1544 at the 45th AIAA Aerospace Sciences Meeting and Exhibit, Reno, NV, 7–10 January 2007; received 17 July 2007; accepted for publication 14 January 2008.

*Graduate Research Assistant, Mechanical and Aerospace Engineering, 4130 Old Main Hill. Member AIAA.

†Assistant Professor, Mechanical and Aerospace Engineering, 4130 Old Main Hill. Associate Fellow AIAA.

λ = clock angle, deg
μ = dynamic viscosity, $N \cdot s/m^2$
μ = true mean
σ = true standard deviation
τ = filter time constant, s
ϕ = cone angle, deg
χ^2 = probability distribution
ω_n = natural frequency of the port response function, rad/s

I. Introduction

FOR the first five decades of human space flight, government space agencies (for example, NASA) have had the exclusive responsibility for development of spacecraft capable of delivering humans into space. However, during the past decade, private organizations have made considerable progress, and space tourism has been projected to be a multibillion industry during the second decade of this century.[‡] On 21 June 2004, the Scaled Composites SpaceShip1 (piloted by Mike Mellville) became the first privately funded spacecraft to break the 100-km barrier to space. SpaceShip1 won the X-Prize with flights on 29 September 2005 (Melville piloting) and on 4 October 2004 (Brian Binnie piloting). Inspired by the X-prize success, several companies have been founded during the past decade with the intention of developing a suborbital-space-tourism market. These companies include Rocketplane-Kistler, Virgin Galactic, Benson Space Company, Space-X Corp., and Xcor Aerospace. These and other suborbital-launch vendors will provide the technologies that will allow the more near-term space-access market to develop.

The various space-access designs for the preceding companies all present differing technology features; however, one common aspect to all of the missions is that the vehicles will exit the atmosphere via rocket power and reenter the atmosphere in an unpowered state. The vehicles must carefully manage reentry conditions and energy levels to insure that load and heating levels are not exceeded and to provide sufficient energy margin to safely reach the landing site under all flight conditions. Most of these designs call for the vehicle to land unpowered on a horizontal runway in a manner similar to that used by the space shuttle. Key phases during the flight include launch, atmospheric interface, and terminal-area energy management. Regardless of the particular design features or mission operations, these transatmospheric vehicles are generally more aircraft than spacecraft, and air-mass reference measurements are required for flight-critical subsystems and uses such as inertial-guidance vertical-channel stabilization, inner- and outer-loop flight control, terminal-area energy management, and ascent winds biasing to keep the angles of attack and sideslip within prescribed limits. Knowledge of the wind-relative vehicle states, dynamic pressure, Mach number, angles of attack and sideslip, altitude, and surface winds for runway alignment is especially critical for the landing phase of the mission.

The hostility of the reentry environment (both heating rates and dynamic pressure levels) precludes the use of permanently deployed probes. Deployable probes (similar to the system installed on the space shuttle) can be used to derive air-data measurements. However, two issues make the probe-based system prohibitively expensive: 1) integration onto the vehicle airframe and 2) system calibration. A more economical and technically viable solution is offered by a flush air-data sensing (FADS) system. The FADS concept, in which air data are inferred from a matrix of nonintrusive surface-pressure measurements, does not require probing of the local flowfield to compute air-data parameters. This innovation allows the high hypersonic heating caused by the small radius of a flow-sensing probe to be avoided and extends the useful range of the air-data measurement system from low-subsonic to the hypersonic flow regime. The FADS system requires no deployment mechanisms and can be integrated directly onto the vehicle nosecap with no movable parts. Because the FADS system does not probe the flowfield but instead uses the natural contours of the forebody, the flowfield is much cleaner and is easier to calibrate. An additional advantage of the FADS system is that it offers the potential to sense air data on ascent, an option not available to the probe-based system. This paper develops the design and simulates the performance of a FADS system for a transatmospheric vehicle based on the X-34 mold lines. Reasons for selecting the X-34 airframe for study will be detailed in Sec. III of this paper.

[‡]Data available online at http://www.space.com/spacetourism/ [retrieved 27 Dec. 2006].

II. Background

The first major effort to collect air data on a hypersonic vehicle was the ball–nose flow-direction sensor on the X-15 rocket-powered research vehicles in 1965 [1,2]. This sensor consisted of four pressure ports attached to pressure transducers, with the ports mounted on a moveable spherical nosecap. The sensor was steered to null the normal and lateral pressure-port differences. By measuring the position of the ball at the nulled position, angles of attack and sideslip could be determined. The cumbersome analog system was prone to hydraulic failures and was required to be dismantled and inspected between flights to insure the integrity of the components. The ball-nose sensor was abandoned when the X-15 project concluded. The shuttle entry air-data system (SEADS) program was proposed in 1980 and used flush pressure ports on the shuttle nosecap to determine flight data at hypersonic and supersonic conditions at Mach numbers significantly greater than those for the shuttle's deployable hemispherical probes. This preliminary concept was tested on a KC-135 in early 1981 [3]. The SEADS was flight-tested on the Columbia orbiter on Mission 61c [4]. In 1987, FADS was qualitatively evaluated on an F-14 [5] at transonic speeds and high angles of attack, to determine system performance for application to general aircraft under a large range of flight conditions. For these early programs, the sensed pressures were related to the desired air-data parameters using a nonphysical mapping. These tests verified the feasibility of the fixed orifice concept but did not demonstrate real-time-capable algorithms for estimating the air data from the pressure measurements.

The first estimation algorithms capable of real-time operation were developed at the NASA Dryden Flight Research Center during the late 1980s for the F/A-18 High-Alpha Research Vehicle (HARV) program. The HARV flight tests also demonstrated that the measurement range of FADS systems could be extended to angles of attack greater than 60 deg. The computations were performed postflight using pressure data telemetered to the ground [6,7]. Failure-detection and fault-management methods were developed in the early 1990s for the same system [8]. The FADS approach was adapted for installation on a wing leading edge in 1993 [9]. This design option allowed for the operation of a FADS system that would not interfere with the fire-control radar system in military vehicles. An analysis of the feasibility and uncertainty associated with using a FADS system under hypersonic conditions was added in 1994 [10]. In 1995, The estimation algorithms developed for the HARV program were demonstrated in a real-time-flight environment on the F/A-18 systems research aircraft [11]. Up to that point, all of the FADS system calculations were performed postflight and were compared with other telemetry data. Cobleigh et al. [12] expanded the calibration technique to apply to generic blunt forebodies in 1998. Crowther et al. [13] detailed their work on calibrating neural networks to interpret pressure data for an arbitrary fuselage design [13]. At roughly the same time, Rohloff et al. [14,15] used neural networks to calibrate flush air-data systems for blunt-nosed configurations.

The FADS system was applied to three premier hypersonic flight programs in the late 1990s: the X-33, X38, and X-43 hypersonic research vehicles. For the X-33 program [16], a FADS system was designed and calibrated in 1998. Unfortunately, the X-33 program was cancelled before the system could be flight-tested [17]. The X-38 system relied on FADS for control system feedback and gain scheduling [12]. The system was evaluated under subsonic flight conditions for multiple test flights conducted between 1996 and 1998. During one drop test, angle-of-sideslip feedback from the FADS system allowed the control system to right the vehicle after it roll-departed following its release from the B-52 carrier aircraft. In 2000, Davis et al. [18] developed a FADS system for use at

supersonic and hypersonic speeds for the X-43 Hyper-X Scramjet demonstration vehicle. The FADS system was intended for later use in the guidance of hypersonic wedge-shaped vehicles. The X-43 system was flown as an experiment to demonstrate the feasibility of operating a FADS system on a sharp-nosed waverider configuration. Pressure data were obtained from launch to the impact for all three X-43 test flights, and the results were analyzed postflight.

III. Selection of Airframe for Simulation

As mentioned in the Introduction, this paper develops a design for and simulates the performance of a FADS system for a transatmospheric vehicle based on the X-34 mold lines. The X-34 was originally conceived as part of a family of experimental vehicles designed to demonstrate technologies that would increase the safety and reliability of future launch vehicles. Key technologies initially planned for demonstration on the X-34 included lightweight composite airframe structures that require little inspection; reusable composite propellant tanks, tank insulation, and other propulsion components; advanced thermal protection systems capable of surviving subsonic flights through rain and fog; integrated (built-in) low-cost avionics, including a differential global positioning system and inertial navigation system; automated vehicle health monitoring and diagnosis; and a conformal air-data system for flight control inputs that would replace traditional probelike air-data sensors.

The X-34 was chosen for this study because the vehicle incorporates many of the features needed by a commercial suborbital-tourist spaceflight system. The X-34 program, cancelled in 2001 when NASA terminated funding for its Space Launch Initiative program [17], has an airframe mold line that was developed using public dollars and the extensive aerodynamic data base is available in the public domain [19–21]. The aerodynamic database includes nose pressure distributions and these data were used for calibration of the candidate FADS system. The aerodynamic database was derived from wind-tunnel testing and computational fluid dynamics analysis. Unfortunately, as with the X-33 program, the X-34 was cancelled before the first flight, and so no actual flight data are available for evaluation of the system. Figure 1 shows a three-view schematic of the original X-34 vehicle.

Figure 2 shows a typical flight profile. Plotted parameters include altitude, downrange, Mach number, velocity, angle of attack, and flight-path angle. During a typical flight operation, the X-34 would be carried to an altitude of approximately 40,000 (12 km) under the belly of a modified L-1011 aircraft and released. After release, the rocket engine would fire and power the vehicle to a peak altitude of approximately 250,000 ft (76 km) and a true airspeed of greater than 7000 ft/s (Mach 7.5). The vehicle reenters the atmosphere at high angles of attack to dissipate energy and then pitches over to achieve normal supersonic flight. This flight profile demonstrates that the X-34 is capable of flying the types of trajectories that would be used by space-tourism operators. To reach the mythical 100-km (320,000 ft) space threshold, speed can easily be traded for altitude.

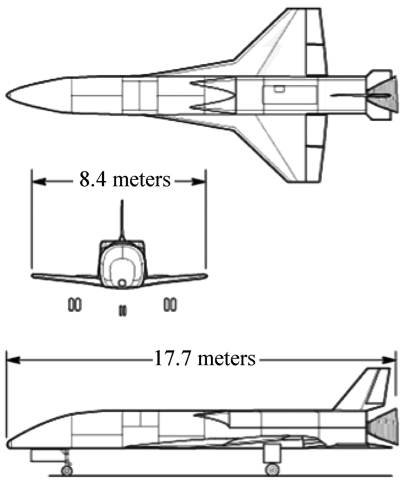

Fig. 1 X-34 vehicle.

IV. Proposed FADS Port Layout and Measurement Architecture

Figure 3 shows the X-34 nosecap and the port locations on the surface. This design reproduces the FADS layout originally specified for the X-34 system. The number of measurements in the pressure matrix was selected as a compromise between the need to accurately measure the flow conditions at the nose and the cost of locating ports on the vehicle. These port locations were selected to give the best sensitivity at the atmospheric interface angle of attack (approximately 25 deg), at which the interface angle is so critical, while still providing good sensitivity at lower angles of attack. The configuration allowed for eight sensing ports: five ports in the angle-of-attack plane and three along the angle-of-sideslip plane. The eighth port on the underside of the nosecap is not used for the FADS estimator and is held in reserve for use by redundancy-management processes. This sensed value also serves as a "sanity check" for the static pressure estimated by the FADS system. The FADS ports are located by their polar coordinates, dubbed as clock λ and cone ϕ angles. These angles, when combined trigonometrically with the local angles of attack and sideslip, give the local flow incidence angle relative to the local surface normal. This trigonometric relationship will be presented in Sec. V.A. Ellsworth and Whitmore [22] presented the port-selection procedure in detail, as well as extensive calibration plots, for the X-34 FADS system.

For this study, the sensor characteristics are modeled based on the original X-34 system baseline. Experience with earlier programs [11] demonstrated that the precision pressure-transducer digital pressure units (Honeywell Defense and Space Electronic Systems Business Division) are well-suited for this task. The particular model assumed for this application is the high-precision altimeter (HPA) transducer series,[§] an absolute-pressure unit intended for altimeter applications. These units provide a linear pressure range from 0 to 17.6 psia (121 kPa). The manufacturer's specified accuracy levels are 0.03% of full scale, giving a minimum accuracy of approximately 0.005 psia (0.06 kPa). The output pressures are fully compensated over a temperature range from −40 to 185°C. The X-34 FADS design assumes that the surface pressures are sensed using remotely located digital pressure transducers that communicate with the flight computers across a single multidrop RS-485 network, with each sensor separately addressed by the mission management computer. Figure 4 shows a schematic of the end-to-end FADS measurement architecture. Surface-pressure impulses are transmitted to the transducers via lengths of pneumatic tubing. Ellsworth and Whitmore [22] presented a viable design for the pressure-port interface with the X-34 nosecap.

V. Monte Carlo Simulation Procedure for Evaluating X-34 FADS System Performance

The end-to-end system performance is impossible to analyze using purely deterministic (explicit) methods. For this study, Monte Carlo simulations are used to evaluate performance the proposed FADS system along a nominal X-34 trajectory. The simulation begins with the nominal flight trajectory and a wind model being algebraically combined to produce a realistic "truth set" of flight conditions. This trajectory is then passed to a pressure-generating subroutine that calculates the surface pressures at each time frame along the flight trajectory. These pressure–time histories are then corrupted with modeled error sources, both systematic and random. Corrupted data used as inputs to the estimation algorithm and air-data estimates are generated along the trajectory. Residuals between estimates and the actual trajectory are evaluated for a large number of simulation runs and rms errors are calculated. The errors are parameterized as functions of Mach number, angle of attack, and altitude and are then plotted. Resulting plots reveal weak points in the

[§]Data available online at http://www.pressuresensing.com/datasheets.html.

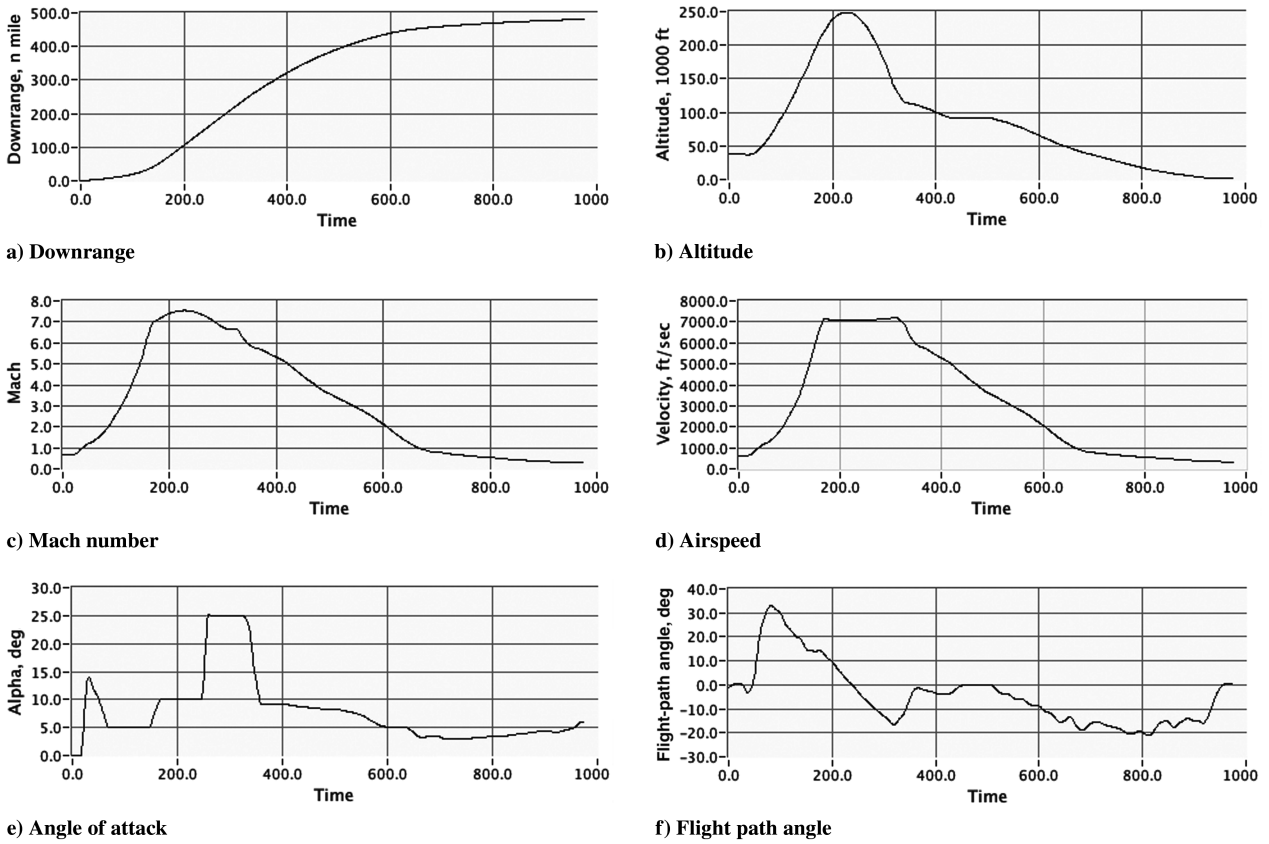

Fig. 2 Typical X-34 flight trajectory.

system design. Figure 5 depicts the Monte Carlo uncertainty analysis procedure used in this study.

Winds are generated for each run using the 1999 global reference atmospheric model (GRAM99) [23]. Wind will, of course, have a significant effect on cross range and downrange, which drives the requirement to calculate the wind-relative (air-data) states. Figure 6 shows a mean January wind profile at 34.9 north latitude and 117.88 west longitude (Edwards Air Force Base, California). A different launch site will have different wind conditions, but this distribution is a representative case. Figure 6 also shows the procedure that was used to combine wind effects with the nominal X-34 flight profile.

A. Simulation of FADS Pressures

The first step in the simulation process is the generation of realistic surface-pressure values for each port location and for each data point along the reference trajectory. For a given trajectory, the independent parameters in the FADS pressure model are 1) angle of attack α, 2) angle of sideslip β, 3) freestream Mach number M_∞, and 4) pressure altitude h_p. Using either the GRAM99 [23] model or the 1976 U.S. standard atmosphere [24], the ambient temperature and pressure are generated along the trajectory. Using the computed value for the ambient pressure and the freestream Mach number, dynamic pressure behind the bow shock wave is generated using standard one-dimensional fluid mechanics relationships [25].

Following the procedure developed by [5–11], the surface pressures are modeled by the equation

$$p_i = q_{c_2}(\cos^2\theta_i + \varepsilon \sin^2\theta_i) + P_\infty \tag{1}$$

where p_i is local surface pressure for port i, q_{c2} is impact pressure, p_∞ is freestream static pressure, ε is a calibration parameter that is

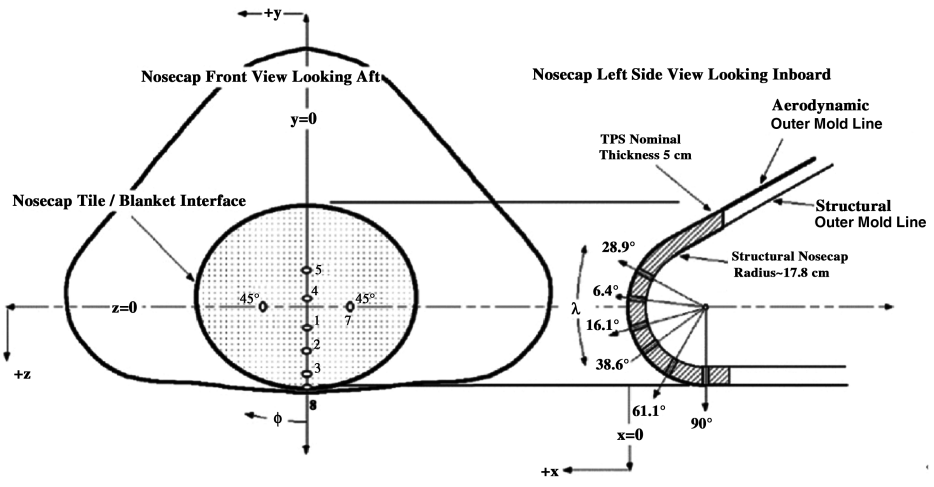

Fig. 3 X-34 nosecap showing chosen pressure-port locations and coordinate definitions.

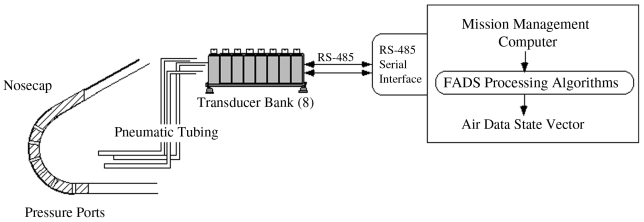

Fig. 4 End-to-end schematic of X-34 FADS signal flow.

prescribed as a function of Mach number and angle of attack, and θ is the flow incidence angle, given by

$$\theta = \cos^{-1}[(\cos\phi)(\cos\alpha)(\cos\beta) + (\sin\phi)(\sin\lambda)(\sin\beta) + (\sin\phi)(\cos\lambda)(\sin\alpha)(\cos\beta)] \quad (2)$$

where the coordinates ϕ and λ are the clock and cone angles of port i. Figure 7 defines the clock- and cone-angle coordinates.

As mentioned previously, the X-34 the calibration coefficient was empirically derived from NASA-sponsored wind-tunnel tests.

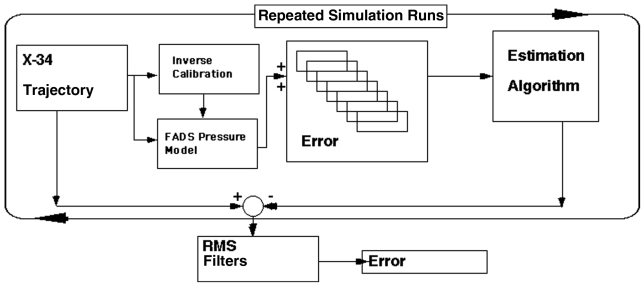

Fig. 5 Monte Carlo simulation procedure.

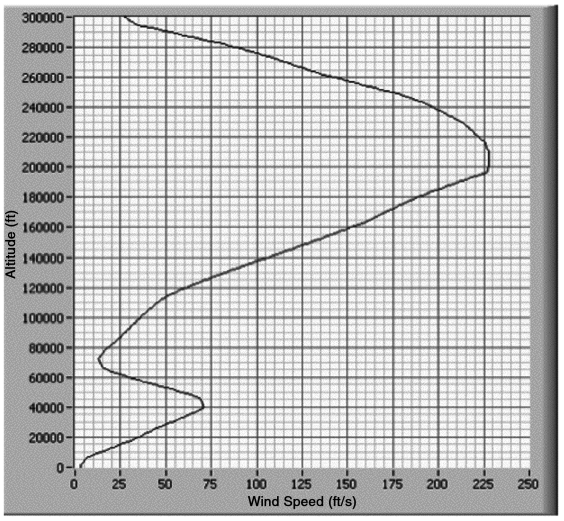

a) Mean January wind profile for Edwards AFB, California

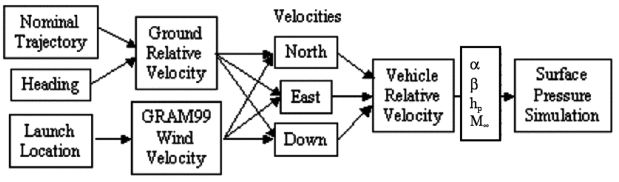

b) Process used to model wind effects in Monte Carlo simulation

Fig. 6 Typical wind profile and procedure for combining wind effects with nominal X-34 trajectory.

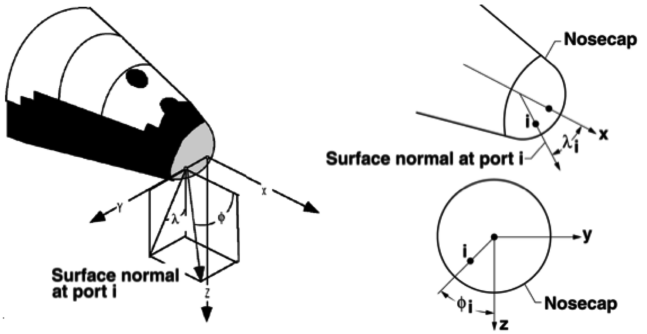

Fig. 7 FADS port coordinate definitions.

Figure 8 shows the variation of ε with respect to Mach number at $\alpha = 0$ for various forebody shapes. The important point to take away from Fig. 8 is that ε approaches zero beyond Mach 2.0. This property makes the FADS insensitive to calibration errors beyond transonic Mach numbers. References [12,22] present detailed calibration plots for the X-34 FADS system.

B. FADS Pressure Error Models

After the ideal surface pressures are calculated using Eqs. (1) and (2), the pressures are corrupted with various error sources to provide the FADS solver algorithm (Sec. VI) with a realistic data set to use for system evaluation. These error models include 1) pneumatic lag; 2) sensor latency; 3) sensor noise, bias, and random; and 4) sensor resolution and truncation error.

The pneumatic-lag routine simulates the response delay of the requisite pneumatic tubing used to plumb the ports to the transducers, and the latency models simulate the processing and communication delays of the pressure transducers. After the application of pneumatic lag and latency sources, the signal is corrupted with random sensor noise and bias error to simulate the behavior associated with real-world transducers. Finally, the transducer resolution is modeled. It is important to note that the noise sources must be applied in the proper order: lag, latency, noise, and then resolution error. If the random noise components are applied first, these noise components will be smoothed out by the pneumatic-lag and latency-filter routines.

Lesser effects not modeled include port misalignment, nonequilibrium gas chemistry, dynamic pressure and thermal deformation of the nosecap, thermomolecular transpiration of pressure tubes (Knudsen number), boundary-layer thickening due to viscous heating, and aerodynamic calibration errors. Nonequilibrium real-gas chemistry and rarefied flow effects become significant for orbital reentry, in which heating levels are extreme; however, the Mach numbers encountered during suborbital reentry are significantly lower and allow these effects to be ignored.

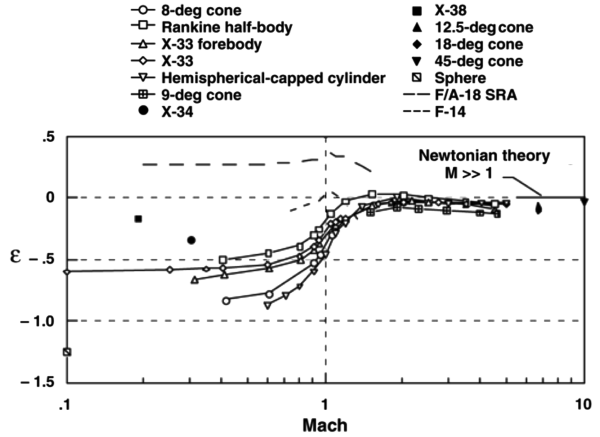

Fig. 8 Variation of ε with Mach number at $\alpha = 0$ for various forebody shapes.

1. Pneumatic-Lag Model

The FADS surface ports are plumbed to the measurement sensors using lengths of tubing, for which frictional losses and wave resonance in the pressure tubing induce spectral distortions that cause both a response lag and a magnitude attenuation. Based on the analysis presented by Whitmore and Moes [7], the pneumatic attenuation effects are modeled by a time-varying second-order system in which the parameters are a function of the tubing geometry and the input pressure value. The second-order frequency-response model is

$$\frac{P_L(\omega)}{P_0(\omega)} = \frac{\omega_n^2}{s^2 + 2\varsigma\omega_n + \omega_n^2} \tag{3}$$

where s is the Laplace variable [26], P_L is the pressure at the downstream end of the pneumatic tubing, and P_0 is the input pressure at the FADS port. The parameter ω_n is the natural frequency, given by

$$\omega_n = \sqrt{\frac{A_c c^2}{LV} \Big/ \left(\frac{L \cdot A_c}{2V}\left[1 + \frac{256}{3}\frac{\gamma}{P_0\rho_0}\left(\frac{\mu \cdot L}{D^2}\right)^2\right] + \left[1 + \frac{512}{3}\frac{\gamma}{P_0\rho_0}\left(\frac{\mu \cdot L}{D^2}\right)^2\right]\right)} \tag{4}$$

and ζ is the damping ratio, given by

$$\varsigma = \frac{\omega_n}{2}\left(128\frac{\mu L}{\pi D^4 P_0}\right)\left(V + \frac{L \cdot A_c}{2}\right) \tag{5}$$

where L is the length of the pneumatic tubing, A_c is the cross-sectional area, D is the tube diameter, V is the volume entrapped in the transducer, μ and γ are the mean viscosity and ratio of specific heats of the gas trapped in the tubing, and ρ_0 is the density of the fluid at the tube entrance.

The important point to take away from Eqs. (4) and (5) is that the natural frequency of the model becomes diminishingly small (narrow response bandwidth) and the damping ratio becomes large as the input pressure and density become small. Thus, pneumatic effects are most significant at high altitudes. Another significant result is that ports near the stagnation region have higher pressure and hence greater frequency-response bandwidth and less latency than pressure ports that lie away from the stagnation point. Conversely, ports away from stagnation region have lower pressure and are hence more damped and have larger pneumatic latencies. These differential latencies can lead to significant computational errors at high altitudes and Mach numbers.

The advantage of having an expression of the form of Eq. (3) is the ease of implementation in the time domain using digital filtering techniques [27]. The modeled pneumatic tubing assumes a diameter of 0.16 cm (1/16 in.) and a length of 152 cm (~5 ft). To allow for random variations in the pneumatic layout and to account for pneumatic modeling errors, the nominal geometric parameters are allowed to vary randomly across the grouping of sensors. These variations are set at the beginning of each Monte Carlo run and are held constant for the remainder of the run. At the beginning of each data frame, the viscosity, local tube density, and sonic velocity are evaluated using the input surface pressure for the port.

2. Sensor Latency Model

As mentioned earlier, this analysis assumes that the Honeywell HPA sensors are grouped together on an RS-485 bus to sense the FADS pressures. This architecture results in a latency in the pressure reporting. For this analysis, it is assumed that the communication will be at the maximum available rate of 28,800 baud. The correct time delay is calculated by adding the transmission time and internal sensor delay. At 28,800 baud, each bit takes 0.0347 ms to clock. Each 10-bit character (1 start, 8 data, 1 stop) takes 0.347 ms. A global pressure request (*99P3) is six characters, including the carriage return. This request commands the sensors to return their data sequentially with a single-character delay between each response. For eight pressure sensors, each command-receive sequence passes a total of

$$6 + (6 + 1) \times 8 = 62 \text{ characters}$$

characters. Thus, with a clocking time of 0.347 ms per character, a single command-receive sequence takes 21.514 ms. The internal processing delay for the transducers (integration time plus digitization delay) is approximately 9.33 ms. Thus, the worst-case end-to-end communication latency is 30.844 ms, and the maximum sample rate for this system is approximately 32.4 samples per second. When the approximate FADS calculation times are taken into account, the actual end-to-end cycle time for each data frame is set at 30 samples per second. Thus, the output latency is approximately 0.0333 s. The total transducer latency (~33 ms) is fed into a first-order filter as a time constant to simulate the delay. Each of the pressure values are filtered using the same latency time constant.

Although this latency may seem insignificant, for reentry conditions, it can result in significant altitude differences between the FADS and inertial systems. For example (referring to Fig. 2), during the atmospheric reentry, the vehicle drops 125,000 ft in approximately 125 s, or a mean altitude rate of −1000 ft/s. Thus, a latency of 0.0333 would amount to an altitude error of approximately 33 ft.

3. Sensor-Noise Model

As mentioned earlier, this analysis assumes that the X-34 FADS pressures are to be sensed by the Honeywell HPA transducers that have a full-scale range of 0 to 17.6 psi and a specified error of less than 0.03% ($3-\sigma$) of full-scale reading (± 0.76 psf). The sensor-error model decomposes the total error into two parts: 1) a bias error that varies randomly among the sensors and is fixed as a function of time and 2) a random error that varies among the sensors and randomly varies as function of time. Common mode bias errors caused by the fundamental accuracy of the reference standard used to calibrate the sensors are assumed to be negligible. The transducer error is divided equally among the bias- and random-error components: $\pm 0.015\%$ $3-\sigma$ ($\pm 0.005\%$ $1-\sigma$) each. As mentioned earlier, the bias-error component is set and held fixed at the beginning of each Monte Carlo run but is allowed to vary randomly among the sensors. The random error is allowed to vary at each call to the error model and varies among the grouping of sensors.

4. Sensor Resolution and Truncation Error Model

The HPA sensors use a 16-bit A/D converter to convert from analog-to-digital signal, and the actual sensor resolution is approximately 0.04 psf (0.002 kPa). This error is insignificant when compared with the random errors applied in the previous subsection. In reality, the RS-485 word length limits the precision of the output parameters, and the HPA rounds the output value to the nearest

0.001 psia (0.007 kPa). This effect is modeled using a custom-designed rounding function.

VI. FADS Solution Algorithm

The original FADS solver algorithms previously developed in [5–11] rely on a nonlinear regression to calculate the air-data states from the pressure inputs. This algorithm had a tendency to be unstable, and data spikes or dropouts would cause the algorithm to diverge [8]. Reference [16] solves this problem by decoupling the highly nonlinear angle-of-attack and angle-of-sideslip solutions from the other air-data state-estimation algorithms. The decoupled solution is referred to as the *triples algorithm* and is the subject of [28]. The triples algorithm, offering a significant improvement to the earlier nonlinear regression approach, solves for the angle of attack and sideslips in polar form and requires the calculation of multiple trigonometric series. The algorithm to be presented in this section follows the triples formulation but solves for the three-axis nondimensional velocity components instead of directly solving for the flow-direction angles. The flow angles are calculated after the three-axis velocity components have been calculated. The result is an algorithm that is computationally more efficient and has a significantly reduced cycle time.

Equation (1) posits that the local surface pressure at any point on a spherelike forebody is a function of the freestream flight conditions, the angle between the effective flow vector and the surface normal, and three calibration parameters $\delta\alpha$, $\delta\beta$, and ε. Together, the four parameters α, β, q_{c_2}, and p_∞ make up the FADS air-data state vector:

$$X_{\text{FADS}} = \begin{bmatrix} \alpha \\ \beta \\ q_{c_2} \\ p_\infty \end{bmatrix} \tag{6}$$

Using these four parameters, most other air-data parameters of interest can be calculated. Because flow incidence angles are imbedded in θ, Eq. (1) is inherently nonlinear and cannot be directly inverted to solve for the air-data vector. By taking strategic differences of three surface-sensor readings (triples), the parameters q_{c_2}, p_∞, and ε are eliminated from Eq. (1). The resulting equation is

$$\Gamma_{ik}\cos^2\theta_j + \Gamma_{ji}\cos^2\theta_k + \Gamma_{kj}\cos^2\theta_i = 0 \tag{7}$$

where

$$\Gamma_{ik} = p_i - p_k, \qquad \Gamma_{ji} = p_j - p_i, \qquad \Gamma_{kj} = p_k - p_j \tag{8}$$

and pressures p_i, p_j, and p_k are the pressures values for ports i, j, and k. Although Eq. (7) is still nonlinear, the complexity is reduced significantly. Rewriting $\cos(\theta)$ in terms of the nondimensional velocity components and the port coordinates gives (ith port)

$$\cos\theta_i = \frac{\begin{bmatrix} X_i & Y_i & Z_i \end{bmatrix}\begin{bmatrix} U \\ V \\ W \end{bmatrix}}{\sqrt{\left(X_i^2 + Y_i^2 + Z_i^2\right)(U^2 + V^2 + W^2)}} = \begin{bmatrix} x_i & y_i & z_i \end{bmatrix}\begin{bmatrix} u \\ v \\ w \end{bmatrix} \tag{9}$$

where X, Y, and Z are the Cartesian coordinates of the pressure ports (Fig. 7); U, V, and W are the components of the air velocity at those points; and x, y, and z and u, v, and w are their respective dimensionless equivalents:

$$\begin{aligned} &u = \cos\alpha\cos\beta, \qquad v = \sin\beta, \qquad w = \sin\alpha\cos\beta, \\ &x_i = \cos\lambda_i, \qquad y_i = \sin\phi_i\sin\lambda_i, \qquad z_i = \cos\phi_i\sin\lambda_i \end{aligned} \tag{10}$$

Substituting Eq. (9) into Eq. (8), taking pressure ratios, and collecting terms gives

$$\begin{aligned} C_{p_{123}} &= \frac{p_1 - p_2}{p_2 - p_3} = \frac{(x_1u + y_1v + z_1w)^2 - (x_2u + y_2v + z_2w)^2}{(x_2u + y_2v + z_2w)^2 - (x_3u + y_3v + z_3w)^2} \\ C_{p_{132}} &= \frac{p_1 - p_3}{p_3 - p_2} = \frac{(x_1u + y_1v + z_1w)^2 - (x_3u + y_3v + z_3w)^2}{(x_3u + y_3v + z_3w)^2 - (x_2u + y_2v + z_2w)^2} \end{aligned} \tag{11}$$

where C_{P123} and C_{P132} are the pressure triples and give the algorithm its name.

A. Angle-of-Attack Estimator

The angle-of-attack solution can be decoupled from the sideslip solution by using only pressures triples aligned along a central vertical meridian ($y = 0$), as depicted in Fig. 7. After extensive algebra, the solution can be written as

$$\tan(\alpha) = \frac{w}{u} = \frac{-B \pm \sqrt{B^2 - 4AC}}{2A} \tag{12}$$

where the coefficients are

$$\begin{aligned} A &= C_{p_{123}}\left(z_3^2 - z_1^2\right) + C_{p_{132}}\left(z_2^2 - z_1^2\right) \\ B &= 2\left[C_{p_{123}}(x_3z_3 - x_1z_1) + C_{p_{132}}(x_2z_2 - x_1z_1)\right] \\ C &= C_{p_{123}}\left(x_3^2 - x_1^2\right) + C_{p_{132}}\left(x_2^2 - x_1^2\right) \end{aligned} \tag{13}$$

Equation (12) has two distinct roots spaced 90 deg apart. This property makes selecting the correct root relatively simple, because under most flight circumstances, the correct root lies closest to the zero angle of attack. If the vehicle is intended to fly at high angles of attack (greater than 45 deg), the correct root can be chosen by comparing the two calculated roots with the inertially determined angle of attack and taking whichever is the closest. As shown in Fig. 2, the maximum planned angle of attack for the X-34 is less than 30 deg, and so a root selection is not an issue for this study. In the unlikely event that $p_2 = p_3$ exactly, then the triples of Eq. (11) approach infinity and Eq. (13) does yield a valid result. In that case, Eq. (11) can be reformulated as

$$(p_1 - p_2)\left[(x_2u + z_2w)^2 - (x_3u + z_3w)^2\right] = 0 \tag{14}$$

and results in an angle-of-attack solution dependent only upon pressure-port location:

$$\tan(\alpha)_{p_2=p_3} = \frac{w}{u} = \pm\left[\frac{x_2 - x_3}{z_3 - z_2}\right] \tag{15}$$

B. Angle-of-Sideslip Estimator

After the local angle of attack has been estimated, the angle of sideslip may then be evaluated using any combinations of the available ports, other than the obvious set in which all three ports lie on the vertical meridian. This generality of the FADS β algorithm offers more choices for β-port locations but also results in a significantly more complex solution. The final result is a quadratic equation in $\tan\beta$ for which the solutions are given by

$$\tan(\beta) = \left(\frac{-B \pm \sqrt{B^2 - 4AC}}{2A}\right)\cdot\cos\alpha \tag{16}$$

where

$$
\begin{aligned}
A &= \tfrac{1}{2}\left[y_1^2 + Cp_{132}y_2^2 + Cp_{123}y_3^2\right] \\
B &= y_1[x_1 + z_1\tan(\alpha)] + Cp_{132}y_2[x_2 + z_2\tan(\alpha)] \\
&\quad + Cp_{123}y_3[x_3 + z_3\tan(\alpha)] \\
C &= \tfrac{1}{2}\Big([x_1 + z_1\tan(\alpha)]^2 + Cp_{132}[x_2 + z_2\tan(\alpha)]^2 \\
&\quad + Cp_{123}[x_3 + z_3\tan(\alpha)]^2\Big)
\end{aligned} \tag{17}
$$

Equations (16) and (17) are valid for any three-port arrangement, except for the degenerate case in which all three ports lie along the central vertical meridian. Because the angle-of-sideslip triples are not required to lie along a single meridian, there is no theoretically limiting relationship between the two roots of Eq. (16). However, practice has shown that there is a wide separation between the two roots. For the low angles of sideslip applicable to this vehicle, the algorithm that selects the roots with a magnitude closest to zero gives the correct root. Whitmore et al. [29] presented a detailed analysis of this root-selection problem. Additionally, the β solution is most accurate when the port arrangement is symmetrically distributed about the central vertical meridian. A nonsymmetrical arrangement of ports makes the solution ill-conditioned and makes the calculation susceptible to noise amplification. Equation (16) is susceptible to the same singularity conditions as the angle-of-attack solution. For the case in which $p_2 = p_3$, the singular solutions are given by

$$
\begin{aligned}
(\tan\beta_1)_{p_2=p_3} &= \cos(\alpha)\left[\frac{[x_3 + z_3\tan(\alpha)] - [x_2 + z_2\tan(\alpha)]}{y_3 - y_2}\right] \\
(\tan\beta_2)_{p_2=p_3} &= -\cos(\alpha)\left[\frac{[x_3 + z_3\tan(\alpha)] + [x_2 + z_2\tan(\alpha)]}{y_3 + y_2}\right]
\end{aligned} \tag{18}
$$

Selecting the root from Eq. (18) that is closest to zero gives the correct result.

C. Triples Averaging

Figure 3 shows that there are five available ports on the vertical meridian for angle-of-attack estimation (excluding the lower port on the underside of the nosecap). The total number of triples available for a given number of ports is given by the binomial coefficient

$$
\binom{n}{k} = \frac{n!}{(n-k)!k!}
$$

where n is the total number of available meridian ports, and $k = 3$ is the number of ports in a triple. Thus, there are a total of 10 triples available for angle-of-attack computations. The FADS algorithm averages the results of these 10 triple calculations for every valid set of triples. The criteria for determining what constitutes a valid triple are discussed in Sec. VII. Averaging the results of the multiple calculations provides for frequency-independent filtering and noise rejection by the FADS algorithm. For the angle-of-sideslip algorithm, only the three symmetrical port arrangements nearest to the vertical centerline of the nosecap are averaged.

D. Static Pressure and Compressible Dynamic Pressure Estimator

After the values of α and β have been calculated using the algorithm of the previous section, then the incidence angles at all of the ports can be evaluated and only ε, p_∞, and qc_2 remain as unknowns in the pressure model. The FADS pressure model is rewritten as a function of p_∞ and qc_2. For n sensed pressures, the resulting $n \times 2$ overdetermined system (more equations than variables) of equations is

$$
\begin{bmatrix} p_0 \\ p_1 \\ p_2 \\ p_3 \\ . \\ . \\ . \\ p_{n-1} \end{bmatrix}
=
\begin{bmatrix} \cos^2\theta_0 + \varepsilon\sin^2\theta_0 & 1 \\ \cos^2\theta_1 + \varepsilon\sin^2\theta_1 & 1 \\ \cos^2\theta_2 + \varepsilon\sin^2\theta_2 & 1 \\ \cos^2\theta_3 + \varepsilon\sin^2\theta_3 & 1 \\ . & . \\ . & . \\ . & . \\ \cos^2\theta_{n-1} + \varepsilon\sin^2\theta_{n-1} & 1 \end{bmatrix}
\begin{bmatrix} qc_2 \\ p_\infty \end{bmatrix}
$$

$$
=
\begin{bmatrix} \Theta_0 & 1 \\ \Theta_1 & 1 \\ \Theta_2 & 1 \\ \Theta_3 & 1 \\ . & . \\ . & . \\ . & . \\ \Theta_{n-1} & 1 \end{bmatrix}
\begin{bmatrix} qc_2 \\ p_\infty \end{bmatrix} \tag{19}
$$

where $\Theta = \cos^2(\theta) + \varepsilon\sin^2(\theta)$. Equation (19) is multiplied on both sides by a diagonal weighting matrix

$$
Q \equiv
\begin{bmatrix} q_0 & 0 & 0 & . & . & 0 \\ 0 & q_1 & 0 & . & . & 0 \\ 0 & 0 & q_2 & . & . & . \\ . & . & . & . & . & . \\ . & . & . & . & q_{n-2} & 0 \\ 0 & 0 & . & . & 0 & q_{n-1} \end{bmatrix}
$$

and solved for the vectors qc_2 and p_∞ using the pseudoinverse (least-squares) method. After considerable simplification, the result is

$$
\begin{bmatrix} qc_2 \\ p_\infty \end{bmatrix}
= \frac{\begin{bmatrix} \sum_{i=0}^{n-1} q_i\Theta_i^2 & \sum_{i=0}^{n-1} q_i\Theta_i \\ \sum_{i=0}^{n-1} q_i\Theta_i & \sum_{i=0}^{n-1} q_i \end{bmatrix}
\begin{bmatrix} \sum_{i=0}^{n-1} \Theta_i q_i p_i \\ \sum_{i=0}^{n-1} q_i p_i \end{bmatrix}}
{\left(\sum_{i=0}^{n-1} q_i\Theta_i^2\right)\left(\sum_{i=0}^{n-1} q_i\right) - \left(\sum_{i=0}^{n-1} q_i\Theta_i\right)^2} \tag{20}
$$

The result can be further simplified to give

$$
q_{c_2} = \frac{\left(\sum_{i=1}^{n} q_i\right)\left(\sum_{i=1}^{n} p_i q_i\Theta_i\right) - \left(\sum_{i=1}^{n} q_i\Theta_i\right)\left(\sum_{i=1}^{n} p_i q_i\right)}{\left(\sum_{i=1}^{n} q_i\Theta_i^2\right)\left(\sum_{i=1}^{n} q_i\right) - \left(\sum_{i=1}^{n} q_i\Theta_i\right)^2} \tag{21}
$$

and

$$
p_\infty = \frac{\left(-\sum_{i=1}^{n} q_i\Theta_i\right)\left(\sum_{i=1}^{n} p_i q_i\Theta_i\right) - \left(\sum_{i=1}^{n} q_i\Theta_i^2\right)\left(\sum_{i=1}^{n} p_i q_i\right)}{\left(\sum_{i=1}^{n} q_i\Theta_i^2\right)\left(\sum_{i=1}^{n} q_i\right) - \left(\sum_{i=1}^{n} q_i\Theta_i\right)^2} \tag{22}
$$

Equations (21) and (22) are the working forms of the solver equations used in the FADS algorithm. The weighting parameters $(q_0, q_1, \ldots, q_{n-1})$ allow a failed pressure to be weighted out of the algorithm with minimal impact on the solution. The q_i terms have a nominal value of 1.0; setting the value of q_i to 0 weights the ith pressure reading out of the algorithm.

E. Mach Number Estimator

After qc_2 and p_∞ are calculated, the Mach number can be computed using one-dimensional fluid mechanics relationships [25]. For subsonic flow conditions, the Mach number can be calculated directly using isentropic flow laws, in which

$$M_\infty = \sqrt{\frac{2}{\gamma-1}\left\{\left[\frac{qc_2}{p_\infty}+1\right]^{\frac{\gamma-1}{\gamma}}-1\right\}} \tag{23}$$

For subsonic flow conditions, $\gamma = 1.4$ is a good working assumption. For supersonic flow conditions, the Mach number can be extracted from a numerical solution of a modified form of the Raleigh pitot equation [30]:

$$\frac{qc_2}{p_\infty} = \left\{\left[\left(\frac{\gamma+1}{2}M_\infty^2\right)^{\left(\frac{\gamma}{\gamma-1}\right)}\right] \Big/ \left[\left(\frac{2\gamma}{(\gamma+1)}M_\infty^2 - \frac{(\gamma-1)}{(\gamma+1)}\right)^{\left(\frac{1}{\gamma-1}\right)}\right]\right\} - 1 \tag{24}$$

Equations (21) and (22) appear to be a closed-form solutions, but because the calibration parameter ε is a function of the Mach number, the terms on the right-hand side of Eqs. (21) and (22) are implicitly a functions of both qc_2 and p_∞, Thus, Eqs. (21) and (22) are actually nonlinear and the solution must be extracted iteratively by including either Eq. (23) or Eq. (24), depending on the flight conditions. Figure 9 depicts the information flow and processing steps within the FADS algorithm. The logic of Fig. 9 fits within the block labeled *estimation algorithm* in the Monte Carlo simulation diagram in Fig. 5.

F. Accounting for Real-Gas Effects

For Mach numbers above 4.0, real-gas effects become significant and cannot be ignored [31]. Because of stagnation-point heating, γ changes significantly across the bow shock wave and is not the nominal value of 1.4. An averaged value for γ across the shock wave is calculated using Eckert's empirical reference temperature [32]:

$$T_{\text{ref}} = T_\infty + \tfrac{1}{2}(T_{a_{\text{wall}}} - T_\infty) + 0.22(T_{02} - T_\infty) \tag{25}$$

where T_{ref} is the reference temperature, $T_{a_{\text{wall}}}$ is the adiabatic wall temperature, T_∞ is the freestream temperature, and $T0_2$ is the stagnation temperature behind the shock wave. The adiabatic wall temperature is evaluated as

$$T_{a_{\text{wall}}} = T_\infty\left[1 + \sqrt[3]{P_r}\frac{\gamma-1}{2}M_\infty^2\right] \tag{26}$$

and the stagnation temperature is evaluated as

$$T_{02} = T_\infty\left[1 + \frac{\gamma-1}{2}M_\infty^2\right] \tag{27}$$

where P_r is the Prandtl number for air: $\mu C_p/\kappa$. For nonideal gas conditions, Eqs. (21–27) are solved iteratively. For each of the iterations, the reference temperature and stagnation pressure behind the shock wave are used to look up the gas properties μ, C_p, κ, and γ using real-gas tables for air [33]. For each iteration, the calibration parameter is evaluated using the current value for Mach number. Fortunately, because pressure is a mechanical quantity and depends primarily upon the mechanical aspects of the flow; influences caused by high-temperature-gas properties are secondary and the simple algorithm presented in this section provides adequate real-gas compensation.

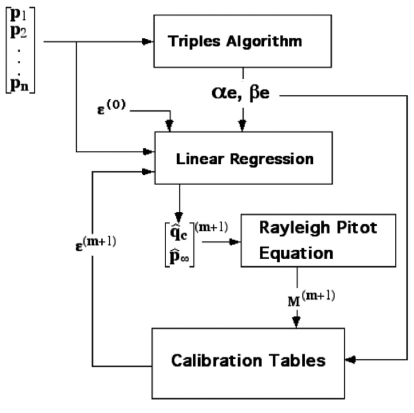

Fig. 9 Flowchart of FADS processing algorithm.

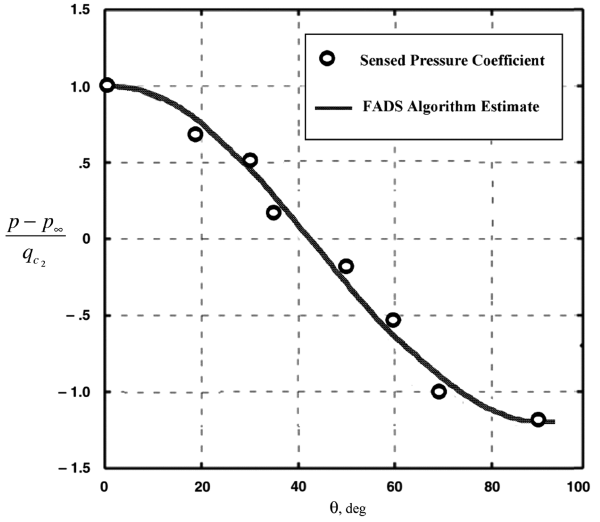

Fig. 10 Surface-pressure coefficient, comparison of sensed and predicted values.

VII. Inertial Enhancement Algorithm

As will be shown in Sec. IX, at high altitudes, the FADS pressure measurements (especially, those away from the stagnation point) have a very low signal-to-noise ratio. This low signal content makes for a very noisy FADS computation. For this reason, air-data measurements are not typically used at altitudes above approximately 25 km (82,000 ft). This section will develop a simple complementary filtering scheme that blends the FADS data with inertially sensed trajectory data. The resulting output is a clean unbiased air-data state-vector estimate. The complementary filtering approach is viable because of the least-squares nature of the FADS algorithm. Figure 10 illustrates this concept, in which the pressure coefficients for the FADS ports are plotted against the surface incidence angle. This figure plots the sensed pressure coefficient as circular symbols and plots the predicted pressure coefficients as a solid line. Clearly, the FADS algorithm has the effect of splitting the differences of the noisy pressure data; that is, the FADS estimate amounts to a curve fit that is unbiased with respect to the input pressure data.

The unbiased nature of the FADS curve fit allows the complementary filter to blend the high-frequency inertial data with the low-frequency FADS data, thereby maintaining the FADS signal fidelity while removing the system noise. Figure 11 presents a block diagram of the inertial enhancement filter (IEF). The filter is written with the angle of sideslip as the state variable, and similar filters exist for the other air-data state variables. The inertially derived beta rate is

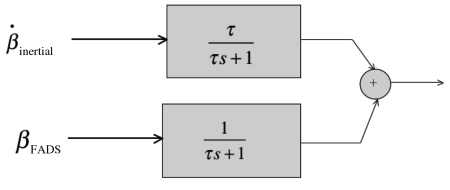

Fig. 11 IEF structure.

high-pass-filtered, the FADS-derived angle of sideslip is low-pass filtered, and the resulting frequency spectra are added. The resulting output value is described mathematically by

$$\beta(s) = \frac{\tau s \beta_{\text{inertial}} + \beta_{\text{FADS}}}{\tau s + 1} = \beta_{\text{inertial}} + \frac{1/\tau}{s + 1/\tau}(\beta_{\text{FADS}} - \beta_{\text{inertial}}) \tag{28}$$

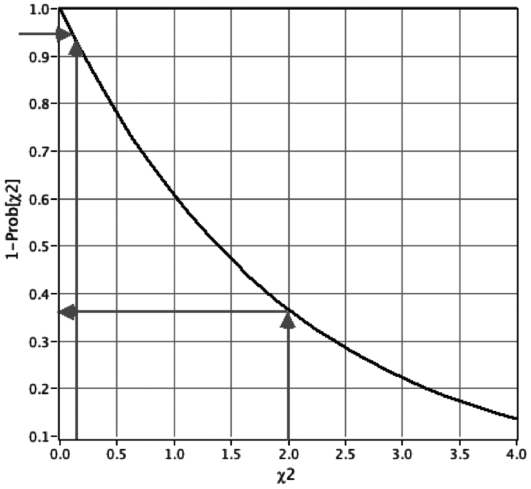

Fig. 12 χ^2 health probability prediction for seven-port FADS system.

This filter can be implemented recursively in the time domain by discretizing Eq. (28) using the bilinear transform with prewarping [27]. The transformation is

$$s = \frac{1}{\tau \tan(\Delta t/2\tau)}\left(\frac{z-1}{z+1}\right) \tag{29}$$

where Δt is the time interval between frames, τ is a time constant that effects the mixture rate between inertial and FADS signals, and z refers to the frame index. For example, $z\ \beta = \beta_{k+1}$, $1/z\ \beta = \beta_{k-1}$, etc., where k is the calculation-time index. The values for τ are scheduled as a function of flight condition, and the scheduling procedure will be discussed in detail in Sec. (IX.C). When Eq. (29) is substituted into Eq. (28) and similar powers in z are collected, the resulting time-domain-difference equation is

$$\beta_{k+1} = \frac{1-\tan(\Delta t/2\tau)}{1+\tan(\Delta t/2\tau)}\beta_k + \frac{1}{1+\tan(\Delta t/2\tau)}\left(\beta_{k+1_{\text{inertial}}} - \beta_{k_{\text{inertial}}}\right) + \frac{\tan(\Delta t/2\tau)}{1+\tan(\Delta t/2\tau)}\left(\beta_{k+1_{\text{FADS}}} + \beta_{k_{\text{FADS}}}\right) \tag{30}$$

where the subscript inertial refers to an inertially derived estimate, the subscript FADS refers to a FADS-derived estimate, and the parameters and β_{k+1} are the filtered estimates at time frames k and $k+1$. The inertial filter effectively uses a weighted average of the current results, the previous frame's results, and inertial data to remove higher-frequency noise from the signal while still retaining the low-frequency

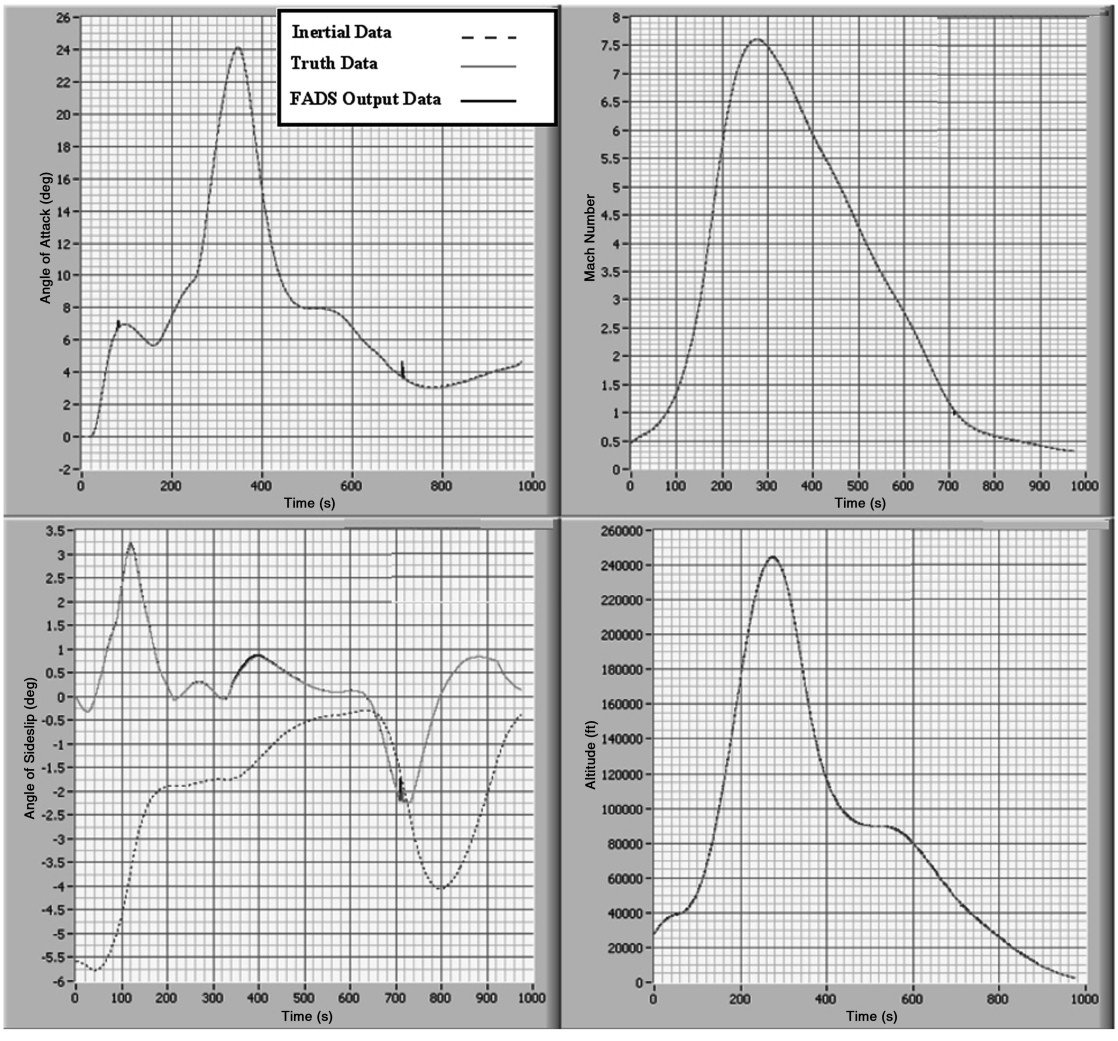

Fig. 13 Self-consistency comparisons for the X-34 FADS algorithm.

components of the FADS estimates. As mentioned earlier, similar filters are employed for angle of attack, altitude, and Mach number output parameters.

In the unlikely case of a full FADS system failure (methods for monitoring the FADS system health will be presented in Sec. VIII.B), a simple method for smoothly transitioning from FADS-derived to inertially derived air data is necessary. The IEFs can be modified to accomplish this task by adding a first-order transitional filter. The resulting difference equation is

$$\beta_{k+1} = \frac{1-\tan(\Delta t/2\tau)}{1+\tan(\Delta t/2\tau)}\beta_k + \frac{1}{1+\tan(\Delta t/2\tau)}\left(\beta_{k+1_{\text{inertial}}} - \beta_{k_{\text{inertial}}}\right) + \frac{A_{\text{wght}}\tan(\Delta t/2\tau)}{1+\tan(\Delta t/2\tau)}\left(\beta_{k+1_{\text{FADS}}} + \beta_{k_{\text{FADS}}}\right) + \frac{(1-A_{\text{wght}})\tan(\Delta t/2\tau)}{1+\tan(\Delta t/2\tau)}\left(\beta_{k+1_{\text{inertial}}} + \beta_{k_{\text{inertial}}}\right) \tag{31}$$

where A_{wght} is a FADS health parameter for which the values can be varied between zero and 1.0. For normal flight operations with a healthy FADS system, $A_{\text{wght}} = 1.0$. The parameter is set to zero in case of a complete FADS system failure. Equations (30) and (31) are new results that have not been previously published in open literature.

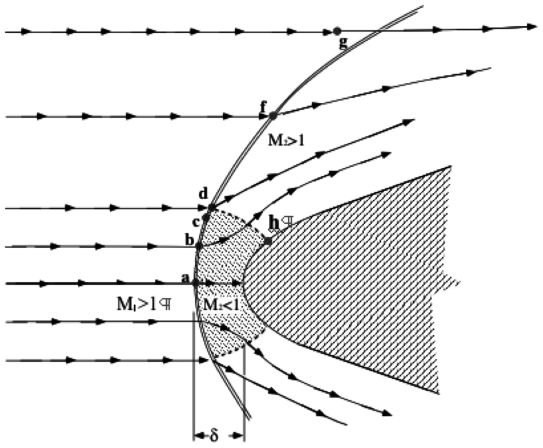

Fig. 14 Transonic flow conditions on the nosecap.

VIII. Fault Detection and Redundancy Management

Figure 4 shows a schematic of the proposed end-to-end FADS architecture for the vehicle. The X-34 vehicle was designed as a single-string system, primarily to keep the development costs within the allotted budget. Thus, the FADS system was a single-string system with respect to communication, busing, and electrical interface. Clearly, because the system was designed to operate as a single string, a single point failure of either the electrical system or the communication bus has the potential to bring the entire system down. At least five pressure measurements are needed to separate the individual air-data parameters. Using more pressure measurements incorporates redundancy into the algorithm and allows for sensors

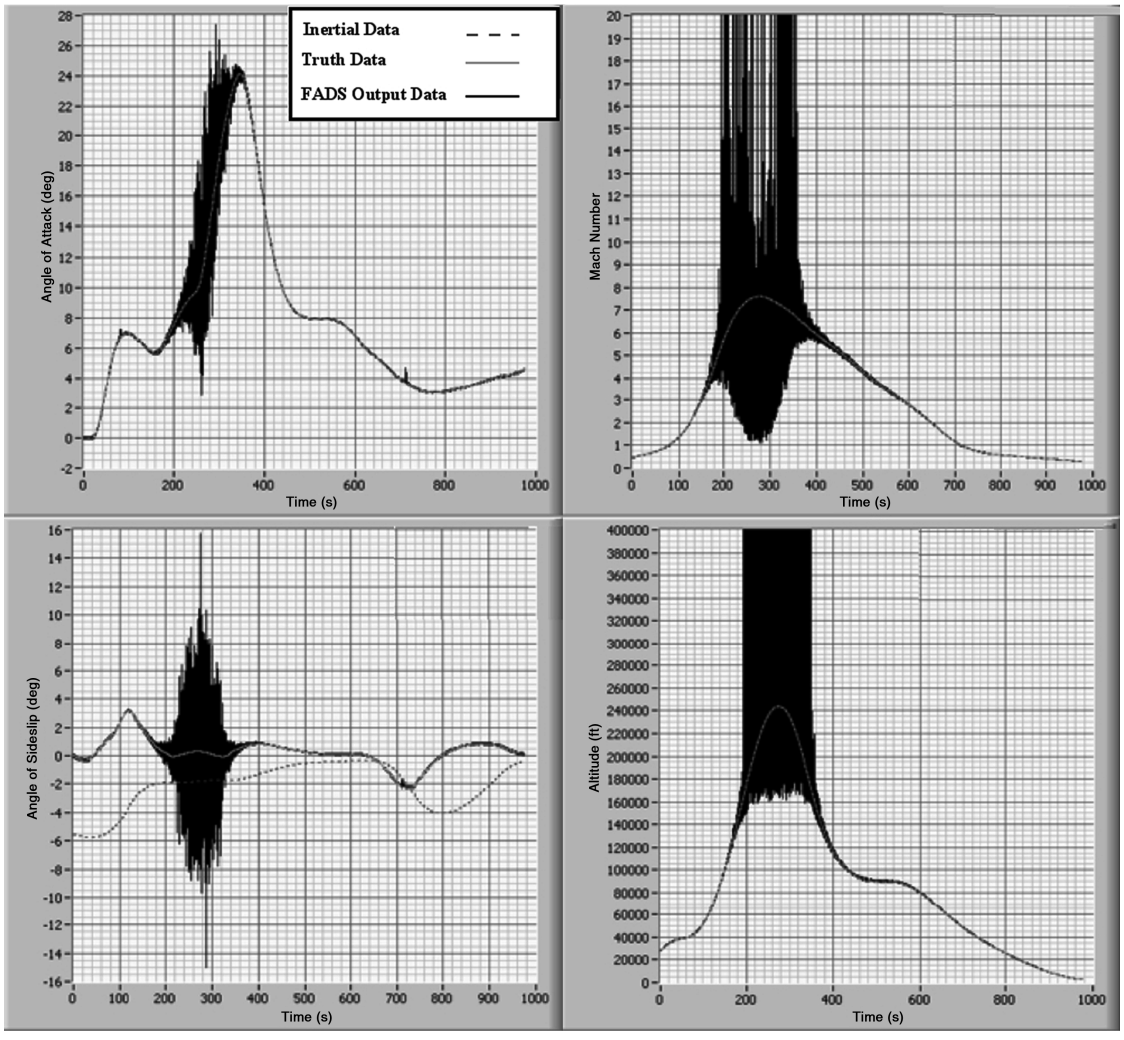

Fig. 15 Effect of noise sources on FADS output.

failures and/or noise rejection. However, the overdetermined FADS pressure matrix with seven ports does provide the opportunity to develop techniques that allowed the system to be partially redundant in terms of failed pressure sensors.

A. Pressure-Reading Validity Checks

When the mission management computer interrogates the sensor matrix, there are three primary data-validity checks that can be performed for the FADS system: 1) data-range test, 2) watchdog-timer test, and 3) data-parity test. With the data-range test, the mission management computer simply checks to see if the pressure-data value is within the required limits (0.001 psia $< p <$ 17.6 psia). The watchdog-timer test checks to verify that the particular sensor has responded within a preset time limit. Finally, the parity check looks at the parity bit output by the sensor and compares it with a calculated parity value (based on the value of the raw 10-bit RS-485 data word). If the sensor passes all three validity checks, then its algorithmic weight is set to 1.0 [Eqs. (21) and (22)] and its value is processed normally through the algorithm. If the data value fails any of the three validity checks, then its weight is set to zero and it is excluded from the algorithm. Any data triple that would use this failed pressure reading is not included in the averaged output for angle-of-attack and sideslip parameters. When a sensor fails, a flag is set so that the mission management computer will know that FADS is operating in a degraded mode.

With this technique, any intermittent failure of a pressure reading will be detected and excluded from further processing. Based on the port architecture shown in Fig. 3, this first line of defense allows for a single sensor failure with little or no degradation in the system performance. As such, the system is fail-operational for a single sensor failure. The algorithm can tolerate two detected sensor failures and still output a degraded air-data set. Depending on which two points fail, this degradation may be small or significant. With this criterion in mind, the X-34 FADS can be considered to be fail-safe with regard to two detected pressure-sensor failures.

B. System Health Monitoring

As mentioned in the previous section, the X-34 FADS system is fail-operational for one detected sensor failure and is fail-safe for two detected sensor failure. The key word here is *detected*. The redundancy-management scheme in which failed sensors (high–low violation, parity error, or watchdog timeout) are weighted out of the calculations works very well for managing a sensor that has failed catastrophically. There are, however, several flight scenarios in which a sensor may fail and not be detected by the three validity checks listed in the previous section. For example, a plugged or frozen port would not immediately show as a system failure. The output from the sensor would continue to be logically correct. But as the spacecraft ascends or descends in altitude or changes velocity, the pressure reading would gradually become increasingly less correct and the air-data calculation would become increasingly more corrupt. A health-monitoring method is needed to indicate that the relative health of the air-data system. This health monitor is based on the methods of χ^2 analysis. In a normally distributed population, if the sample variance, represented by

$$s^2 = \frac{\sum_{i=0}^{n-1}(x_i - \mu)^2}{n-1} \tag{32}$$

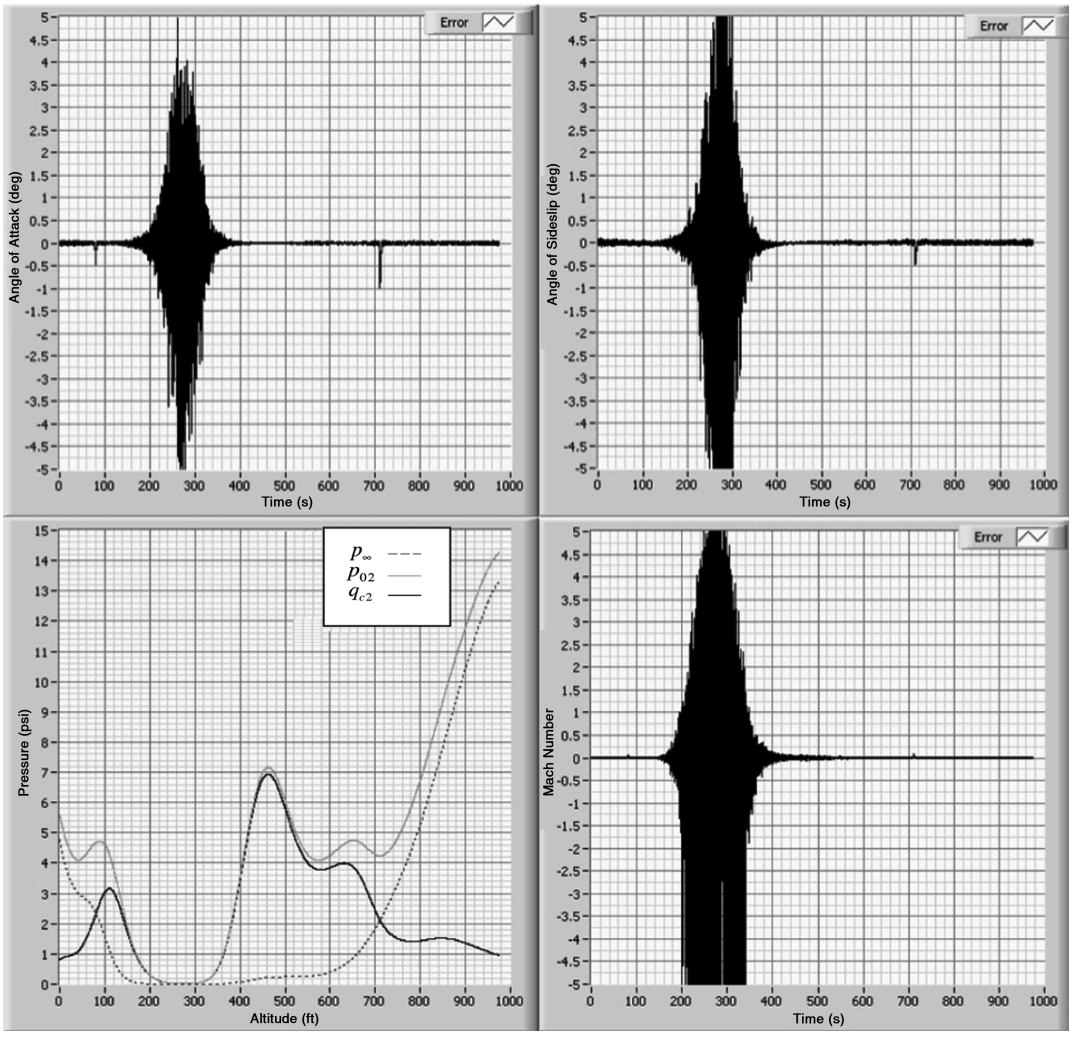

Fig. 16 Measurable pressure difference and its effect on the FADS system output noise level.

is normalized by multiplying by $(n-1)/\sigma^2$, then the resulting parameter is a random number for which the probability distribution is approximately χ^2:

$$\frac{n-1}{\sigma^2}s^2 \approx \chi^2 \rightarrow \text{prob}[\chi^2] = \int_0^{\chi^2} \frac{(-\frac{1}{2}x)^{\frac{\kappa-2}{2}}}{2^{\kappa/2}\Gamma(\kappa/2)} e^{(-\frac{1}{2}x)}\,dx \qquad (33)$$

where κ is equal to the degrees of freedom minus 1, Γ is the gamma function, and x is the randomly distributed variable. For n random numbers selected from a completely independent population, there are $n-1$ degrees of freedom. For each parameter that relates the individual member selected from the random population, the degrees of freedom are reduced by one.

As presented by Whitmore and Moes [8] at the end of each data frame (calculation cycle), the differences between the sensed and calculated pressure values (residuals) are approximately normally distributed with a zero mean value when the FADS system is healthy and functioning properly. Thus, the variable defined by

$$\chi^2_{\delta p} = \sum_{i-0}^{n-1} \frac{\{p_i - (qc^2[\cos^2\theta_i + \varepsilon\sin^2\theta_i] + p_\infty)\}^2}{\sigma^2_{\delta p}} \qquad (34)$$

must be distributed as a χ^2 variable with $n-5$ degrees of freedom. The degrees of freedom are reduced by four because the residuals are related by the four air-data states α, β, qc_2, and p_∞. Thus, for a seven-port system, the parameter of Eq. (34) should be distributed as a χ^2 variable with two degrees of freedom. If the optional eighth port on the underside of the nosecap is included, then the degrees of freedom would be three.

In general, the higher the value of $\chi^2_{\delta p}$ computed from Eq. (34), the worse the system is performing. To test the hypothesis that the system is healthy and performing properly, we compare the parameter $\chi^2_{\delta p}$ against tables of χ^2 for two or three degrees of freedom. If one plots 1-prob[χ^2] versus χ^2, then $\chi^2_{\delta p}$ can be used to predict the relative health of the system; Fig. 12 demonstrates this concept. For the seven-port example, there are two degrees of freedom, and a value of $\chi^2_{\delta p} = 2.0$ indicates only a 36% probability that the system is healthy and functioning properly. In contrast, a value of $\chi^2_{\delta p} = 2.0$ indicates a 95% probability that the system is healthy and functioning properly.

One can perform this hypothesis test because the value for σ^2 is constructed a priori from modeled residuals for a system that is healthy and functioning properly. The expected error for each of the sensor readings is on the order of 0.03% of full-scale reading. Based on a full scale of 17.6 psia, the expected sensor error is ± 0.76 psf (0.0365 kPa). Thus, for seven sensors, the sum-mean-squared pressure error should be approximately 4.05 psf^2. This error is sum-squared with the calibration and other systematic errors to give the expected residual sum-squared error for the system. For now, assume that the calibration error is twice the 0.03% full-scale sensor error at approximately 1.52 psf (0.073 kPa). Thus, the expected error in any sensor reading is approximately ± 1.7 psf (0.08 kPa). For a 95% health indicator, we want

$$\frac{n-1}{\sigma^2}s^2 \approx \chi^2 \rightarrow \sigma^2 = \frac{n-1}{\chi^2}s^2 = \frac{(7-1)\cdot 1.7}{0.2} = 51 \text{ psf}^2 \qquad (35)$$

Assuming that the values for the other sensors are near the mean value of ± 0.76 psf, then because

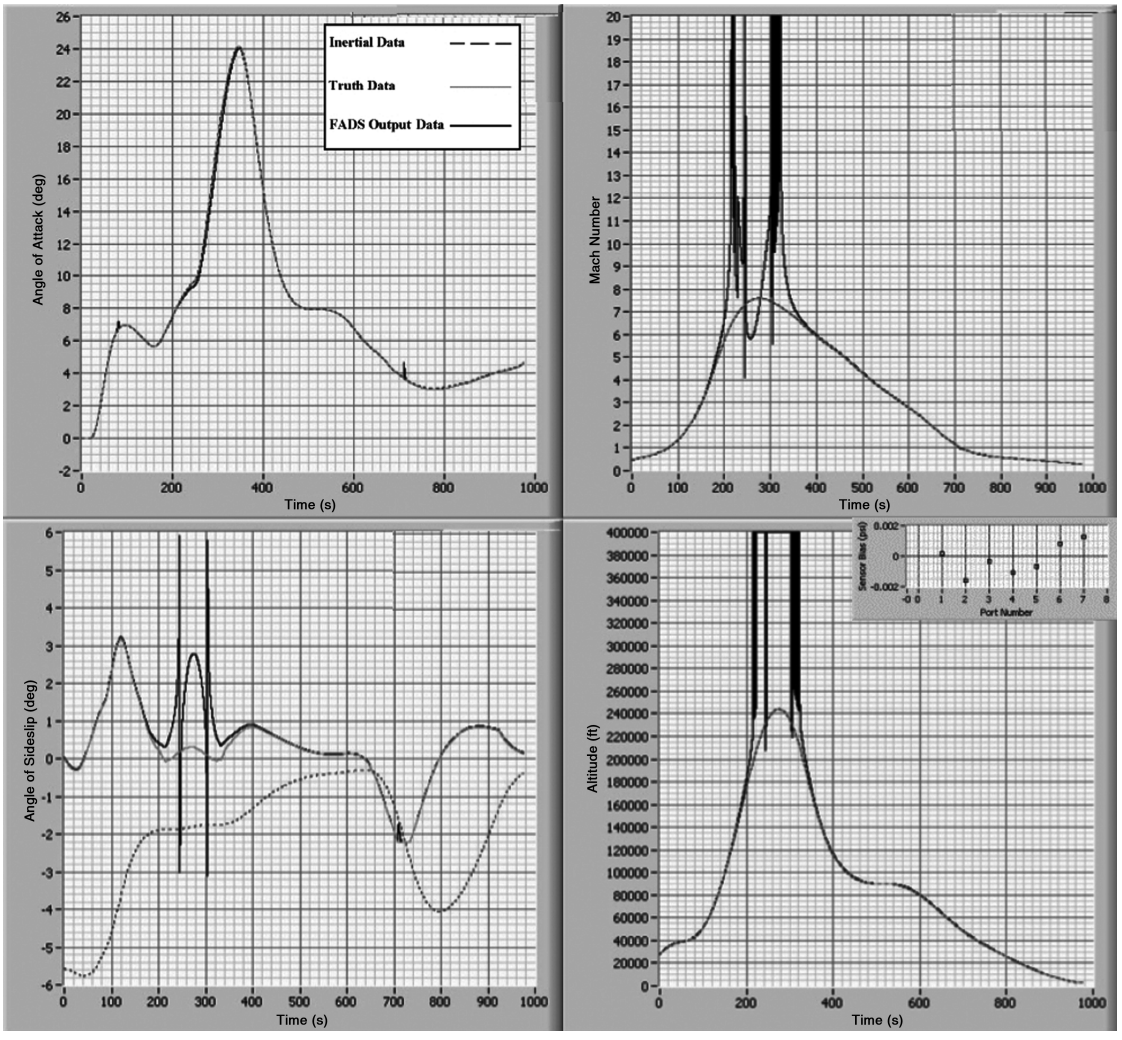

Fig. 17 Effect of sensor bias errors on FADS output.

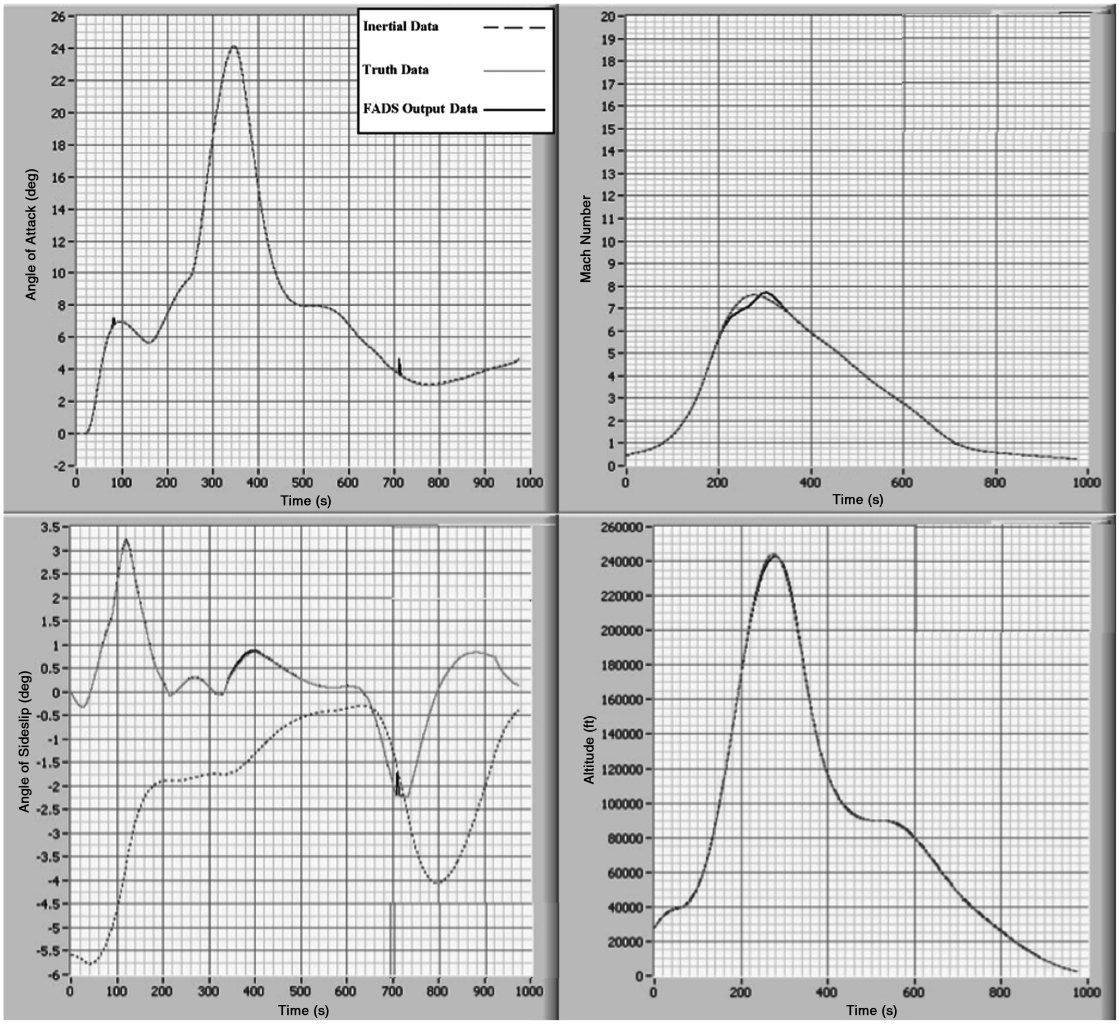

Fig. 18 Effect of pneumatic lag on FADS output.

$$\sigma^2 = \frac{1}{n-1}\sum \delta p^2$$

a single sensor would have to present an error of

$$\delta p_{\max} = \sqrt{(n-1)\sigma^2 - \sum_{i=1}^{6} \delta p_i^2} = \sqrt{(7-1)\cdot 51 - 6\cdot(0.75^2)}$$
$$= \pm 17.4 \text{ psf } (0.83 \text{ kPa}) \tag{36}$$

to trip the χ^2 error flag. This value corresponds to approximately 7% of full scale (a fairly conservative value). It is important to set the $\chi^2_{\delta p}$ failure threshold low enough to allow true error detection and high enough to avoid nuisance error flags.

C. Application of FADS Health Monitoring Parameter for FADS Redundancy Management

Evaluating the $\chi^2_{\delta p}$ parameter as a part of the FADS algorithm calculation allows the system health to be easily and quickly monitored. Assuming that a single pressure value has caused the χ_2 failure flag to trip, this technique allows the isolation of a bad (but undetected) pressure port by sequentially weighting out individual ports. When the bad port has been weighted out of the algorithm, the computed $\chi^2_{\delta p}$ value will drop dramatically, isolating the bad sensor in the system.

IX. Simulation Results

This section presents the results of the Monte Carlo simulation analyses. Self-consistency tests are performed first. Next, the error models described earlier are superimposed on the pressure data and the resulting FADS calculations are compared against the truth data. Finally, the inertial enhancement filter is included in the simulation and is used to stretch the range of operability of the FADS system to very high altitudes.

A. Self-Consistency Verification

The first step in the Monte Carlo simulation process is to validate that the FADS algorithm is self-consistent. That is, use the X-34 trajectory and FADS pressure model to generate the simulated pressure data, and then input that data to the FADS solver algorithm.

Table 1 Nominal and transonic coefficients for determining τ from the logistical growth equation

Filter	A_{mp1}	R	C	c_1	n	A_{mp2}	c_2
Alpha	75	$-1/15,000$	200,000	0.5	2	−5000	50
Beta	75	$-1/15,000$	200,000	0.5	4	5000	0.05
Mach and altitude	10,000	$-1/8000$	200,000	0.5	2	−5000	25

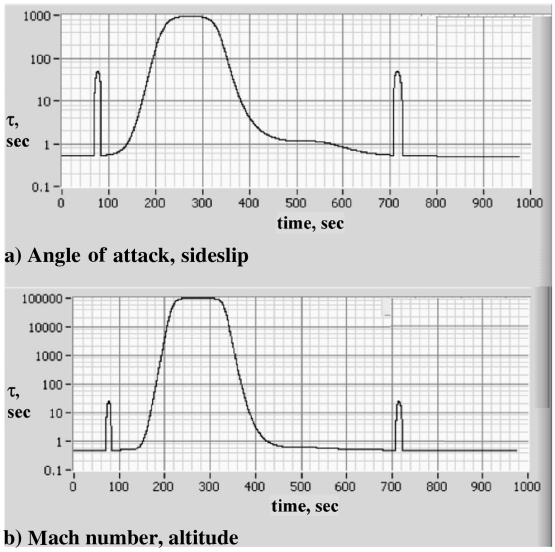

Fig. 19 Inertial filter time-constant scheduling for nominal X-34 reentry.

These output air-data states are compared against the original trajectory values; Fig. 13 presents these comparisons. These plots display the inertial, truth, and estimated air-data parameters. Except for spikes in angle of attack and sideslip that occur at the sonic condition, the truth and estimated air-data states agree to a very high degree of accuracy. The spikes in angle of attack and sideslip are the result of instabilities at the transonic point caused by the movement of the Mach line across the nosecap; Fig. 14 illustrates this event. In this case, some of the ports are exposed to subsonic flow and some of the ports are exposed to supersonic flow. The line between points d and h is the line at which $M = 1$. Port locations both fore and aft of point h are under two different flow regimes, and the triples algorithm is not able to account for this via the simplified FADS pressure model. This blip is an inescapable component of all previously designed air-data systems, both FADS and conventional. Fortunately, time spent in transonic conditions is short, and stable solutions are rapidly attained after the transonic point. As will be shown in Sec. IX.C, the IEFs will be used to significantly diminish the effects of this transonic blip.

B. FADS System Performance with Pressure Error Present

Having demonstrated in the previous section that the FADS algorithm is self-consistent along the X-34 trajectory, the simulation runs are repeated with the previously discussed pressure error sources superimposed on the simulated pressure data. Figure 15 shows a typical time-history comparison for a single Monte Carlo run. By comparing time scales, it can be seen that the system becomes very noisy above a 100,000-ft (30.5-km) altitude and is effectively useless above a 150,000-ft (45.7-km) altitude. Interestingly, at high altitudes, the error in the FADS calculations becomes large when the impact (dynamic) pressure behind the shock wave drops below 1.0 psf (0.048 kPa). Figure 16 demonstrates this result, in which the residual time histories in angle of attack, sideslip, and Mach number

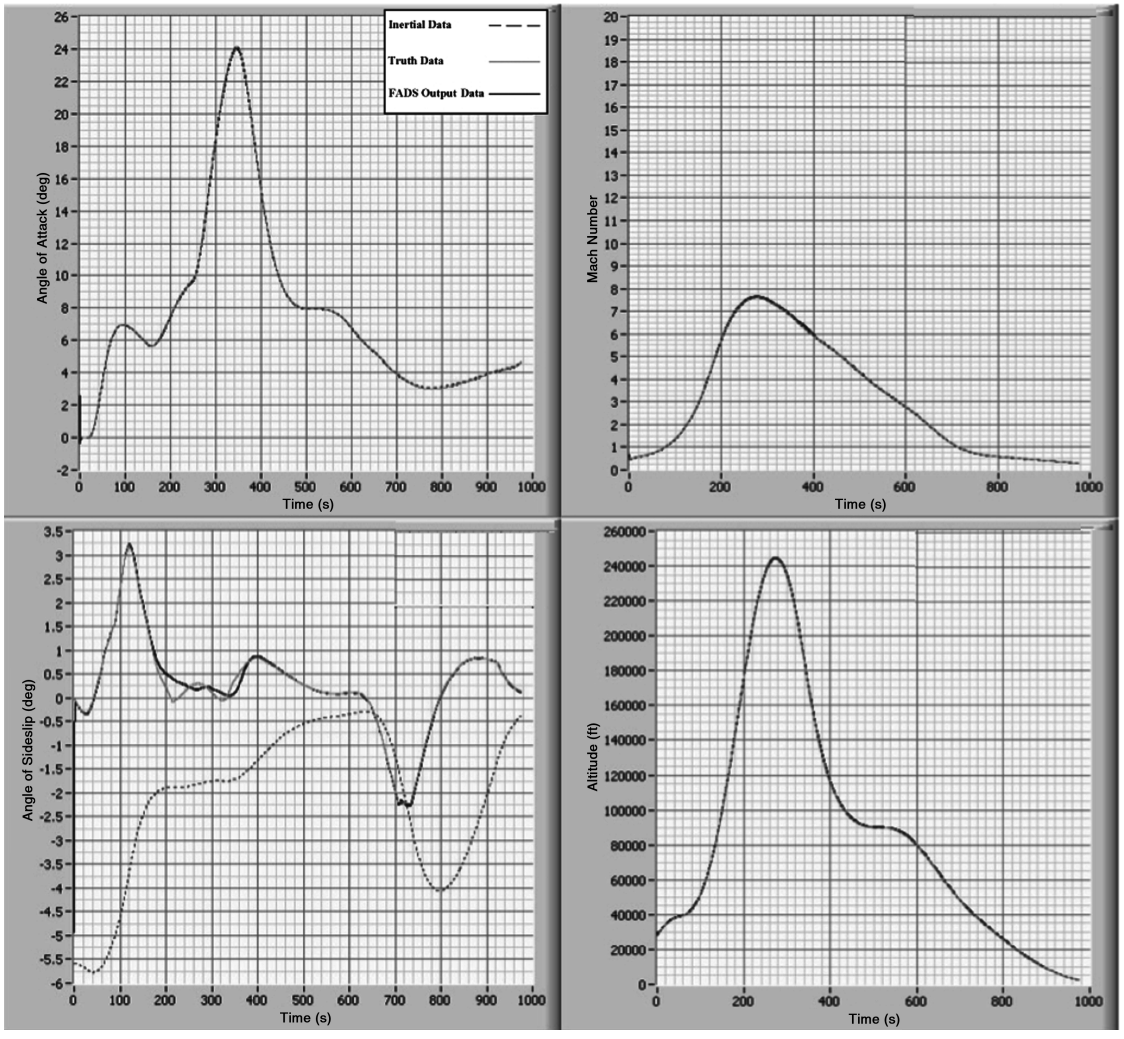

Fig. 20 Fads calculations with inertial enhancement filters active.

Table 2 Statistical analysis for 1000 runs with all error sources active

	Response without inertial enhancement filtering			Response with inertial enhancement filtering		
	Alpha, deg	Sideslip, deg	Mach	Alpha, deg	Sideslip, deg	Mach
Mean residual	−0.08848	−0.13588	0.24212	−0.01048	−0.03714	−0.00807
Standard deviation	1.2253	2.03697	6.51938	0.04293	0.18729	0.01999
Root mean square	1.22849	2.0415	6.52387	0.04419	0.19094	0.02156

are plotted with the truth time histories for p_∞, p_{02}, and q_{c2}. Thus, it is the sensed impact pressure and not the ambient pressure level that has the dominant effect on the system performance in the presence of pressure-measurement noise or error sources.

The major error source contributing to the very noisy FADS outputs at low-impact pressure levels displayed in Figs. 15 and 16 is the random noise in the pressure measurements; however, the sensor bias and pneumatic lag also contribute to the poor performance. Figures 17 and 18 show the contributions of sensor bias error and pneumatic lag to the FADS output errors for a typical Monte Carlo simulation run. For this simulation run, the corresponding bias errors are shown in pounds per square inch as an inset figure on the altitude plot of Fig. 17. The effects of the sensor bias error do not become significant until altitudes above 150,000 ft (45.7 km). The effects of the pneumatic lag in the sensor tubing do not become significant until altitudes exceeding 180,000 ft (54.9 km), and these effects only appear in the Mach number and altitude calculations. The sensor-measurement latency and resolution have a far less significant effect on the FADS output error and are not shown here

C. Effects of the Inertial Enhancement Filter

Results presented in the previous subsection demonstrate that the major contributors to the FADS algorithm divergence at low-impact pressure are the random errors in the sensor measurements. Sensor bias errors and pneumatic-lag effects contribute to the error to a significantly lesser extent. Thus, the IEFs, which have a low-pass effect on the FADS data, should offer a significant improvement of the system performance. Furthermore, because the noise effects vary so greatly with altitude and impact pressure, if the filter time constants τ are scheduled as a function of altitude and inertial Mach number, then the maximum amount of wind-relative (pressure-based) signal can be retained while still allowing sufficient noise rejection. For this implementation, the time-constant scheduling follows a logistical growth equation [34] of the form

$$\tau = \frac{A_{\text{mp1}}}{1 + \exp(R(A - C))} + c_1 \tag{37}$$

where A_{mp1} is a multiplication factor, R is the growth rate, A is the current population (altitude in this case), C lies on the altitude axis at the middle of the transition between minimum and maximum values of τ, and the c_1 constant is used to shift the weighting scheme along the τ axis to give greater flexibility in scheduling. A secondary equation is used to correct the transonic instabilities:

$$\tau = A_{\text{mp2}}(M_{\text{inertial}} - 1)^n + c_2 \tag{38}$$

Equation (38) has the effect of forcing the scheduled t to spike up in the vicinity of Mach 1. Selecting the greater of the time constants calculated by Eqs. (36) and (37) gives the correct filter time constant. The coefficients for each filter are given in Table 1. Figure 19 plots the scheduled time constants for the reentry trajectory presented in Fig. 2.

Applying the inertial enhancement filters with the time constants scheduled in this manner significantly reduces the FADS output noise over the entire flight envelope. Figure 20 shows this result for a typical Monte Carlo run. The FADS outputs very nearly reconstruct the truth set. The only exception is with the angle of sideslip at high altitudes, for which the heavy reliance on inertially derived sideslip measurements results in an offset due to upper-level winds. All things considered, the resulting signal would be easily usable by vehicle systems for energy management, navigation, and flight control.

Applying the inertial filtering algorithm has a dramatic effect on the end-to-end system accuracy. Table 2 compares the statistical results of 1000 Monte Carlo runs with and without active inertial filtering. More than an order-of-magnitude reduction in the residual errors is observed for the angle-of-attack and sideslip calculations. The Mach number residual is reduced by more than two orders of magnitude by the enhancement filter.

X. Conclusions

This paper develops design architecture for, and simulates the performance of, a FADS system for a transatmospheric vehicle based on the X-34 mold lines. The X-34 was chosen for this design because it incorporates many of the features needed by a commercial suborbital-tourist spaceflight system. Additionally, the X-34 has an extensive aerodynamic database that is available in the public domain. A preliminary system design is presented, including port layout, measurement architecture, calibrations, processing algorithms, and redundancy-management methods.

Monte Carlo simulations evaluate the performance of the proposed FADS system along a nominal trajectory. Here, representative pressures are calculated and then corrupted by modeled error sources, both systematic and random. The corrupted pressure data are used as inputs to the estimation algorithm, and air-data estimates are generated along the trajectory. Residuals between estimates and the actual trajectory are evaluated for a large number of runs. Root-mean-square-error statistics of the residuals are calculated and represent the achievable system accuracy.

The Monte Carlo simulations demonstrate that the low signal-to-noise ratio of the sensed pressure data at low-impact pressures and high altitudes results in algorithm divergence beginning at altitudes around 100,000 ft. With the use of a simple set of inertial enhancement filters, the useful operating range of the FADS system is extended to altitudes well above 250,000 ft. The enhancement algorithm relies on a simple complementary filtering scheme that blends the FADS data with inertially sensed trajectory data. The result is a clean, mostly unbiased, air-data estimate. The complementary filtering approach is viable because of the least-squares nature of the FADS algorithm that has the effect of splitting the differences of the noisy pressure data.

Because the noise effects on the FADS system vary so greatly with altitude and impact pressure, the enhancement filter time constants are scheduled as a function of altitude and inertial Mach number using a logistical growth equation. The result is an algorithm that retains the maximum wind-relative (pressure-based) signal while still allowing significant noise rejection. The resulting blended algorithm output results in an order-of-magnitude reduction in the residual errors for the angle-of-attack and sideslip calculations. The Mach number residual error is reduced by more than two orders of magnitude by the enhancement filter. The significant outcome of this analysis is that the usable ceiling for air-data systems was extended to altitudes and Mach numbers that can accommodate reentry and atmospheric interface while still providing accurate results for low-altitude operations. The availability of wind-referenced trajectory data throughout the entire endoatmospheric flight path (including launch, reentry, approach, and landing) offers a greatly extended set of options for reentry vehicle guidance, control, and energy management.

References

[1] Cary, J. P., and Keener, E. R., "Flight Evaluation of the X-15 Ball-Nose Flow-Direction Sensor as an Air-Data System," NASA TN D-2923, 1965.

[2] Wolowicz, C. H., and Gossett, T. D., "Operational and Performance Characteristics of the X-15 Spherical, Hypersonic Flow Direction Sensor," NASA TN D-3070, 1965.

[3] Larson, T. J., and Siemers, P. J., III., "Subsonic Tests of an All-Flush-Pressure-Orifice Air Data System," NASA TP 1871, 1981.

[4] Henry, M. W., Wolf, H., and Siemers, Paul M., III., "An Evaluation of Shuttle Entry Air Data System (SEADS) Flight Pressures—Comparisons with Wind Tunnel and Theoretical Predictions," 15th AIAA Aerodynamic Testing Conference, San Diego, CA, AIAA Paper 88-2052, May 1988.

[5] Larson, T. J., Whitmore, S. A., Ehernberger, L. J., Johnson, J. B., and Siemers, P. J., III., "Qualitative Evaluation of a Flush Air Data System at Transonic Speeds and High Angles of Attack," NASA TP 2716, 1987.

[6] Whitmore, S. A., Moes, T. R., Larson, T. J., "Preliminary Results from a Subsonic High Angle-of-Attack Flush Airdata Sensing (HI-FADS) System: Design, Calibration, and Flight Test Evaluation," NASA TM-101713, 1990.

[7] Whitmore, S. A., and Moes, T. R., "The Effects of Pressure Sensor Acoustics on Airdata Derived from a High-Angle-of-Attack Flush Airdata Sensing (HI_FADS) System," NASA TM-101736, 1991.

[8] Whitmore, S. A., and Moes, T. R., "Failure Detection and Fault Management Techniques for a Pneumatic HI-FADS System," NASA TM-4335, 1992.

[9] Whitmore, S. A., Moes, T. R., Czerniejewski, M. W., and Nichols, D. A., "Application of a Flush Airdata Sensing System to a Wing Leading Edge (LE_FADS)," NASA TM 104267, 1993.

[10] Whitmore, S. A., and Moes, T. R., "Measurement Uncertainty and Feasibility Study of a Flush Airdata System for a Hypersonic Flight Experiment," NASA TM 4627, 1994.

[11] Whitmore, S. A., Davis, R. J., and Fife, J. M., "In-Flight Demonstration of a Real-Time Flush Airdata Sensing (RT_FADS) System," NASA TM 104314, 1995.

[12] Cobleigh, B. R., Whitmore, S. A., Haering, E. A. Jr., Borrer, J., and Roback, V. E., "Flush Airdata Sensing (FADS) System Calibration Procedures and Results for Blunt Forebodies," NASA TP-209012, 1999.

[13] Crowther, W. J., Lamont, P. J., and Laurence, D. R. P., "Neural Network Approach to the Calibration of a Flush Air Data System," *The Aeronautical Journal*, Vol. 105, No. 1044, 2001, pp. 85–95.

[14] Rohloff, T. J., Whitmore, S. A., and Catton, I., "Air Data Sensing from Surface Pressure Measurements Using a Neural Network Method," *AIAA Journal*, Vol. 36, No. 11, Nov. 1998, pp. 2094–2101.

[15] Rohloff, T. J., Whitmore, S. A., and Catton, I., "Fault-Tolerant Neural Network Algorithm for Flush Air Data Sensing," *Journal of Aircraft*, Vol. 36, No. 3, May–June 1999, pp. 541–549.

[16] Whitmore, Stephen A., Cobleigh, Brent R., and Haering, Edward A., "Design and Calibration of the X-33 Flush Airdata Sensing (FADS) System," NASA Dryden Flight Research Center TM-1998-206540, Edwards AFB, CA, Jan. 1998.

[17] David, L., "NASA Shuts Down X-33, X-34 Programs" [online article], *Space.com*, http://www.space.com/missionlaunches/missions/x_33_cancel_010301.html [retrieved 28 Dec. 2006].

[18] Davis, M. C., Pahle, J. W., White, J. T., Marshall, L. A., Mashburn, M. J., and Franks, R., "Development of a Flush Airdata Sensing System on a Sharp-Nosed Vehicle for Flight at Mach 3 to 8," NASA TM-209017, 2000.

[19] Pamadi, B. N., Brauckmann, G. J., Ruth, M. J., and Fuhrmann, H. D., "Aerodynamic Characteristics, Database Development, and Flight Simulation of the X-34 Vehicle," *Journal of Spacecraft and Rockets*, Vol. 38, No. 3, May–June 2001, pp. 334–340.

[20] Brauckmann, G. J., "X-34 Vehicle Aerodynamic Characteristics," *Journal of Spacecraft and Rockets*, Vol. 36, No. 2, Mar. 1999, pp. 229–239.

[21] Cobleigh, B. R., Whitmore, S. A., Haering, E. A. Jr., Borrer, J., and Roback, V. E., "Flush Airdata Sensing (FADS) System Calibration Procedures and Results for Blunt Forebodies," 15th AIAA International Space Planes and Hypersonic Systems and Technologies, Norfolk, VA, AIAA Paper 99-4816, Nov. 1999.

[22] Ellsworth, J. C., and Whitmore, S. A., "Reentry Air Data System for a Suborbital Spacecraft Based on X-34 Design," 45th AIAA Aerospace Sciences Meeting and Exhibit, Reno, NV, AIAA Paper 2007-1544.

[23] Justus, C. G., and Johnson, D. L., "The NASA MSFC Global Reference Atmospheric Model: 1999 Version (GRAM-99)," NASA TM-1999-209630, 1999.

[24] Anon., "U.S. Standard Atmosphere, 1976," National Oceanic and Atmospheric Administration, Washington, D.C., 1976.

[25] Anderson, J. D., *Modern Compressible Flow with Historical Perspective*, 3rd ed., McGraw–Hill, Boston, 2003, Chap. 3.

[26] Franklin, G. F., and Powell, J. D., *Digital Control of Dynamic Systems*, Addison–Wesley, Reading, MA, 1980, Chap. 3.

[27] Otnes, R. K., and Enochson, L., *Applied Time Series Analysis*, Wiley, New York, 1978, pp. 219–260.

[28] Whitmore, S. A., Cobleigh, B. R., and Haering, E. A., "Stable Algorithm for Estimating Airdata from Flush Surface Pressure Measurements," U.S. Patent No. 6253166, issued 26 June 2001.

[29] Whitmore, S. A., Cobleigh, B. R., and Haering, E. A., "Design and Calibration of the X-33 Flush Airdata Sensing (FADS) System," NASA Dryden Flight Research Center TM-1998-206540, Edwards AFB, CA, Jan. 1998.

[30] Shapiro, Ascher H., *The Dynamics and Thermodynamics of Compressible Fluid Flow*, Vol. I, Wiley, New York, 1953, pp. 83–88, 154.

[31] Whitmore, Stephen A., and Moes, Timothy R., "Feasibility and Uncertainty Analysis for a Flush Airdata System on a Hypersonic Flight Test Experiment," AIAA Paper 94-1930, June 1994.

[32] Mills, Anthony, F., *Heat Transfer*, Irwin, Homewood, IL, 1992, Chap. 4.

[33] Hansen, C. Frederick, "Approximations for the Thermodynamic and Transport Properties of High-Temperature Air," NASA TR-50, 1959.

[34] Freiberger, W. F., ed., *The International Dictionary of Applied Mathematics*, Van Nostrand, Princeton, NJ, 1960, pp. 552–553.

M. Miller
Associate Editor